

See discussions, stats, and author profiles for this publication at: <https://www.researchgate.net/publication/46217735>

# Solvent-Dependent Spectral Diffusion in a Hydrogen Bonded "Vibrational Aggregate"

ARTICLE *in* THE JOURNAL OF PHYSICAL CHEMISTRY A · OCTOBER 2010

Impact Factor: 2.69 · DOI: 10.1021/jp106142u · Source: PubMed

---

CITATIONS

36

READS

18

## 3 AUTHORS, INCLUDING:



[Carlos Baiz](#)

University of Texas at Austin

40 PUBLICATIONS 406 CITATIONS

[SEE PROFILE](#)

# Solvent-Dependent Spectral Diffusion in a Hydrogen Bonded “Vibrational Aggregate”

John T. King, Carlos R. Baiz, and Kevin J. Kubarych\*

Department of Chemistry, University of Michigan, 930 North University Avenue, Ann Arbor, Michigan 48109

Received: July 2, 2010; Revised Manuscript Received: August 13, 2010

Two-dimensional infrared spectroscopy (2DIR) is used to measure the viscosity-dependent spectral diffusion of a model vibrational probe,  $\text{Mn}_2(\text{CO})_{10}$  (dimanganese decacarbonyl, DMDC), in a series of alcohols with time scales ranging from 2.67 ps in methanol to 5.33 ps in 1-hexanol. Alcohol–alkane solvent mixtures were found to produce indistinguishable linear IR spectra, while still demonstrating viscosity-dependent spectral diffusion. Using a vibrational exciton model to characterize the inhomogeneous energy landscape, several analogies emerge with multichromophoric electronic systems, such as J-aggregates and light-harvesting protein complexes. An excitonic, local vibrational mode Hamiltonian parametrized to reproduce the vibrational structure of DMDC serves as a starting point from which site energies (i.e., local carbonyl frequencies) are given Gaussian distributed disorder. The model gives excellent agreement with both the linear IR spectrum and the inhomogeneous widths extracted from 2DIR, indicating the system can be considered to be a “vibrational aggregate.” This model naturally leads to exchange narrowing due to disorder-induced exciton localization, producing line widths consistent with our 1D and 2D measurements. Further, the diagonal disorder alone effectively reduces the molecular symmetry, leading to the appearance of Raman bands in the IR spectrum in accord with the measurements. Here, we show that the static inhomogeneity of the excitonic model with disorder successfully captures the essential details of the 1D spectrum while predicting the degree of IR activity of forbidden modes as well as the inhomogeneous widths and relative magnitudes of the transition moments.

## I. Introduction

A solute in a hydrogen bonding solvent experiences rapid, discrete fluctuations in the number of hydrogen bonds it makes with the nearest solvent molecules. When those fluctuations induce appreciable changes in a spectroscopically observed transition frequency, multidimensional methods such as two-dimensional infrared (2DIR) spectroscopy are able to measure the correlation function of the frequency fluctuations.<sup>1–13</sup> A key challenge for visible and infrared spectroscopy is the link between actual molecular dynamics and accessible spectroscopic observables, such as frequencies, transition moments, and frequency correlation functions. For systems such as the amide I band of peptides and proteins,<sup>14–18</sup> and the OH (or OD) stretch of liquid water, it has become possible to predict 2DIR spectra using classical dynamics simulations.<sup>19–24</sup> Such simulations guide the atomistic interpretation that is otherwise lacking from the frequency correlation function, which necessarily confounds the actual molecular dynamics and how those dynamics modulate the probed transition. The instances for which frequency mapping methods have been so successful are characterized by being either essentially local modes (e.g., OH/OD and nitrile<sup>25–30</sup>) or by having relatively weak coupling between local modes (e.g., amide I transition dipole coupling). Very recently, extensive progress has been made in treating the complex coupled dynamics of pure liquid water using vibrational exciton models as well as electrostatic maps based on ab initio quantum chemistry.<sup>24,31,32</sup> There has been less extensive consideration of single, strongly coupled extended vibrational chromophores, which should also be sensitive to subtle long- and short-range interactions. It is a desirable feature of a dynamical probe to respond not only to local fluctuations, but also to be sensitive

to correlated fluctuations as would be expected in a cooperative hydrogen bonded environment.

To assess the value of such a spatially distributed probe, we have undertaken a systematic study of the ultrafast vibrational dynamics of the metal–carbonyl complex dimanganese decacarbonyl ( $\text{Mn}_2(\text{CO})_{10}$ , DMDC) in a series of hydrogen bonding alcohol solvents. Due to their amphiphilic nature, alcohols exhibit complex liquid structure characterized by hydroxyl aggregation,<sup>33–36</sup> and given its ~1 nm length and extensive vibrational delocalization, DMDC is an attractive probe of the heterogeneous solvent environment. From Fourier transform IR (FTIR) and waiting-time-dependent 2DIR spectra, we extract homogeneous and inhomogeneous spectral widths as well as time constants for spectral diffusion.

We find that with increased alkyl chain length, the inhomogeneous width narrows, and the time scale for spectral diffusion slows. With the aid of a vibrational exciton model incorporating Gaussian disorder, the data are interpreted in terms of the flexibility of the hydrogen bonded network responsible for the spectral inhomogeneity and its dynamical evolution. On the basis of the ability of the model to reproduce the solvent-dependent absorption spectra while identifying several features shared with electronic aggregates, we suggest that it is appropriate to view the extended delocalized complex as a “vibrational aggregate.”<sup>24,37,38</sup> This analogy immediately facilitates identification of such phenomena as exchange narrowing<sup>39,40</sup> and exciton localization as characterized by measures such as the participation ratio.<sup>38,41,42</sup>

The simple model, which includes only local site disorder, also correctly predicts that site energy disorder alone induces IR activity of otherwise IR-inactive modes. That is, the symmetry can be sufficiently broken without explicit geometric distortion. Last, the model allows straightforward incorporation

\* Corresponding author. E-mail: kubarych@umich.edu.

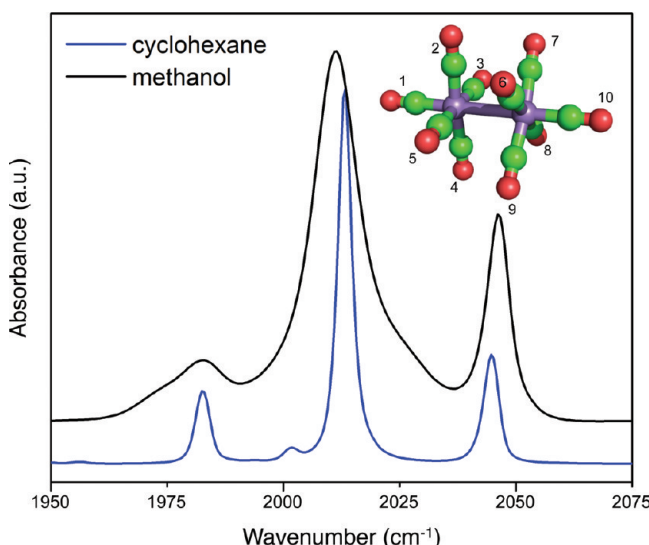


**Figure 1.** FTIR spectra of DMDC in cyclohexane and methanol. The cyclohexane spectrum shows homogeneously broadened lineshapes, and the methanol spectrum shows complex, inhomogeneously broadened lineshapes. Inset shows the structure of the vibrational probe DMDC and the numbering of the carbonyl sites used for the vibrational exciton Hamiltonian.

of site energy correlations in anticipation of the correlated rearrangements of the hydrogen bonded network solvating the probe.<sup>13,43</sup> We find that the nature of the site energy correlations have signatures that, in principle, could be extracted from experimental 2DIR data and compared with atomistic simulations.

**Delocalized Vibrational Probe: Mn<sub>2</sub>(CO)<sub>10</sub>.** We have previously studied the photochemistry and coherent dynamics of dimanganese decacarbonyl using a variety of multidimensional IR methods.<sup>44–48</sup> In all of these studies, the solvent was chosen to yield an essentially homogeneously broadened set of coupled vibrations to maintain the maximum spectral resolution. DMDC (Figure 1 inset) is a highly symmetric molecule consisting of 10 strongly coupled carbonyl units, belonging to an uncommon symmetry point group of  $D_{4d}$ . For this particular point group, each vibrational mode of DMDC is either IR- or Raman-active, with no vibrational modes that have both IR and Raman activity. The four IR-active transitions (Figure 1) occurring at 1983, 2014, 2014, and 2045  $\text{cm}^{-1}$  have  $B_2$ ,  $E_1$ ,  $E_1$  and  $B_2$  symmetry respectively. The modes of DMDC are highly delocalized vibrations involving the collective motion of 8 ( $E_1$  modes) and 10 ( $B_2$  modes) carbonyl units. The high- and low-frequency  $B_2$  vibrational modes can be described by the symmetric and antisymmetric stretches of the axial carbonyls with respect to the equatorial carbonyl units, with transition dipoles that are parallel to the Mn–Mn bond.

The two  $E_1$  modes involve the motion of only the equatorial carbonyls, with mutually perpendicular transition moments that are perpendicular to the Mn–Mn bond (see Supporting Information for animations of all modes).<sup>47</sup> The four IR transitions can be seen in the linear IR spectrum of DMDC in cyclohexane (Figure 1), where the small peak at 2005  $\text{cm}^{-1}$  is a band due to natural abundance <sup>13</sup>C in the complex. The FTIR spectrum of DMDC in cyclohexane (Figure 1) shows transitions that are well characterized by homogeneously broadened Lorentzian lineshapes. In polar solvents, the strong system–bath coupling results in inhomogeneous broadening, but several dark modes also gain significant IR activity (Figure 1). For metal carbonyl complexes, it is common to observe broadening as well as new peaks emerging with increased solvent polarity, where the new

bands often correspond to dark or Raman-active vibrations. Below, we introduce a vibrational exciton model that can account for the appearance of new spectral bands without any explicit geometric distortion or changes to the off-diagonal Hamiltonian matrix elements; instead, they can be attributed to fluctuations that break the energetic symmetry of the molecule. The dynamic symmetry-breaking results in Raman active modes’ (classified by no zero-disorder IR activity) gaining IR oscillator strength and becoming bright in the FTIR spectrum.

**DMDC as a Vibrational Aggregate.** For moderate to strong coupling, it is common to represent the system in a site basis, including the coupling between the sites as off-diagonal matrix elements of the Hamiltonian.<sup>37,49</sup> In the diagonal representation, the states are denoted excitons and generally exhibit some degree of delocalization among the sites. The incorporation of energetic disorder in those site energies (so-called “diagonal” disorder) often leads to localization of the resulting eigenstates. In coupled electronic aggregates, for example, such localization can significantly alter the rates and efficiencies of charge and energy transfer processes. Delocalized systems, such as light-harvesting proteins,<sup>50–52</sup> J-aggregates,<sup>53–57</sup> and conducting polymers,<sup>58</sup> have been extensively studied due to the interest in long-distance charge separation and transport.

Although coupled vibrational systems are routinely described using excitonic Hamiltonians, DMDC displays striking manifestations of a range of phenomena that have long been observed chiefly in coupled electronic chromophores. The highly delocalized vibrational modes of DMDC serve as a vibrational analogue of electronic chromophore aggregates, where delocalization across individual vibrational sites occurs as a function of the bath coordinates. Environmental fluctuations modulate the site energies, thus influencing the coupling and extent of vibrational delocalization. In general, the bath causes disorder-induced localization,<sup>59</sup> where large fluctuations can dislodge a given site from the delocalized network. The extent to which an exciton is distributed over local chromophores can be quantified using the participation ratio, which provides the number of individual units that compose the eigenstate.<sup>60</sup> Spectral lineshapes (either optical or vibrational) have been shown to be sensitive indicators of the participation ratio, in which a higher degree of delocalization naturally leads to narrower lineshapes than would be expected for a given site energy distribution, a phenomenon known as exchange narrowing.<sup>38,39,61</sup> Effects identical to those seen in electronic systems, such as exchange narrowing and disorder-induced localization, are observed and modeled for DMDC in linear alcohol solvents.

Finally, the excitonic nature of the DMDC vibrations enables the molecule to sense nanometer-scale length correlations in the solvation shell, providing a perspective that extends beyond the vicinity of a single solvent molecule. Using the excitonic model, we find that correlations between site energy fluctuations have clear signatures in the inhomogeneous widths of the resulting exciton bands. Since the present model is nondynamical and considers only the static ensemble of transitions, the full utility of this approach and its predictions will be realized once it is combined with a molecular dynamics simulation and a local mode frequency map. Nevertheless, as has been shown in numerous examples, a static description of the energy landscape and the correlations among structural units can provide key insight in applications ranging from peptides to molecular aggregates.

**Spectral Diffusion.** In linear and nonlinear infrared spectroscopy, the analysis of spectral features, including peak position, shape, intensity, evolution, etc., provides insight into

the underlying molecular structures and dynamics.<sup>14,62,63</sup> In the condensed phase, the analysis of spectral features in linear IR spectroscopy is particularly challenging due to constant fluctuations of an inhomogeneous environment, leading to a distribution of transition frequencies that depend on the bath coordinates. Time-resolved spectroscopies based on photon–echo experiments have allowed for the direct observation of the dynamic frequency fluctuations that underlie inhomogeneously broadened line shapes. The static distribution of transition frequencies in systems with strong system–bath coupling can easily be seen using linear IR spectroscopy, but the dynamic features are difficult to discern due to the lack of time resolution in frequency domain spectroscopies. Two-dimensional infrared spectroscopy (2DIR) monitors the correlation between excitation and detection frequencies as a function of waiting time as the system undergoes stochastic fluctuations that modulate the transition frequency. This correlation produces a signature line shape in the 2D spectrum that evolves as the system undergoes environmental fluctuations. The purely absorptive 2DIR spectrum is the sum of real parts of the rephasing (echo) and nonrephasing spectra.<sup>63–65</sup> In the presence of inhomogeneous broadening, the rephasing spectral amplitude is enhanced relative to the nonrephasing spectrum by strong correlation between excitation and detection frequencies. This imbalance in signal amplitudes relaxes as the system explores all the available microscopic environments. The time-dependent correlation of excitation and detection frequencies is described by the frequency–frequency correlation function, which can be extracted from 2DIR spectra through the inhomogeneity index  $I(t)$ ,<sup>66</sup>

$$I(t) = \frac{A_{\text{rephasing}} - A_{\text{nonrephasing}}}{A_{\text{rephasing}} + A_{\text{nonrephasing}}} \quad (1)$$

where  $A$  is the amplitude of the rephasing or nonrephasing peak amplitudes (for single transitions). Monitoring this ratio as a function of waiting time allows the frequency–frequency correlation function (FFCF) to be experimentally extracted for systems whose frequency correlations are slower than the dephasing time, a condition that is satisfied in the metal carbonyl system studied here. From the FFCF, the homogeneous and inhomogeneous contributions to the total line width can be separated using the initial correlation function value combined with the full width at half-maximum (fwhm) of the 1D IR spectrum.<sup>1</sup> Our goal in the present work is to investigate the correlation between translational diffusion—typically parametrized by the viscosity—and the rate of spectral diffusion. The viscosity of a linear alcohol increases monotonically with length,<sup>67</sup> whereas the global hydrogen bond structure is much more weakly length-dependent, as discussed below.

A commonly used model for the FFCF consists of a motionally narrowed term as well as a sum of exponential terms:<sup>1,68,69</sup>

$$C_1(t) = \langle \delta\omega_{01}(t) \delta\omega_{01}(0) \rangle = \frac{\delta(t)}{T_2} + \sum_i \Delta_i^2 \exp\left(\frac{-t}{\tau_i}\right) \quad (2)$$

The first term in eq 2 describes the motionally narrowed portion of the correlation function, where  $T_2$  incorporates pure dephasing, population relaxation, and orientational relaxation into the correlation function, which are considered to be waiting-time-independent. This term, usually dominated by the dephas-

ing of the system caused by extremely fast structural fluctuations, does not contribute to the time evolution of the 2D line shape or the ratio of magnitudes of the rephasing and nonrephasing signals. The second term is the sum over all inhomogeneous terms that contribute an exponential decay to the FFCF, where  $\tau_i$  is the spectral diffusion time constant. For systems with no measurable inhomogeneous broadening, such as a vibrational probe in a weakly interacting solvent, there is no measurable spectral diffusion, and the correlation function consists of only the delta function in the first term in eq 2, corresponding to the effectively constant transition frequency for the band. The correlation function  $C_1(t)$  describes the  $0 \rightarrow 1$  transition autocorrelation function, but note that the  $1 \rightarrow 2$  autocorrelation function as well as the  $0 \rightarrow 1$ ,  $1 \rightarrow 2$  cross correlation function also contributes to the third order response function.

For systems that have inhomogeneous broadening, the homogeneous portion will not contribute to the observed exponential decay of the FFCF. By fully characterizing the inhomogeneous contributions to the correlation function, the dynamics of specific interactions can be isolated. In the case of DMDC in alcohol solvents, there are two distinct limiting solvation environments: hydrogen bonded environments and noninteracting alkyl environments, although the sample is a complicated heterogeneous mixture of the two. Simple alkyl environments would contribute only to the motionally narrowed term of the correlation function, whereas the hydrogen bonded environments are responsible for the exponential decay. Because the inhomogeneous broadening is caused exclusively by the hydroxyl groups of the alcohol, the hydrogen bond dynamics of the system can be selectively studied despite the lack of preferential solvation. The high solubility of DMDC in both polar and nonpolar solvents assures that the bulk solution will not be enhanced by phase separation upon addition of the solute, making DMDC a nonperturbative probe to the natural solvent environment.

In this study, we observe the spectral diffusion of a strongly coupled vibrational probe DMDC in a series of linear alcohol solvents. The hydrogen bonded environment leads to significant spectral broadening, the extent of which is damped by exchange narrowing. In addition, large magnitude fluctuations of local coordinates that participate in the delocalization network cause dynamic vibrational exciton localization. This localization acts to break the energetic symmetry of the vibrational molecule, resulting in Raman-active vibrational modes gaining IR intensity as well as the splitting of previously degenerate modes.

## II. Experimental and Simulation Methods

**2DIR.** The experimental implementation of chirped-pulse upconversion detected 2DIR spectroscopy has been described in detail elsewhere.<sup>70–72</sup> Briefly, a sequence of three fields,  $E_1$ ,  $E_2$ , and  $E_3$  with wave vectors  $\mathbf{k}_1$ ,  $\mathbf{k}_2$ , and  $\mathbf{k}_3$ , separated by times  $t_1$  and  $t_2$  arrive at the sample in a box geometry producing fields  $E_{\pm}$ , emitting during  $t_3$  with wave vectors  $\mathbf{k}_{\pm} = \pm \mathbf{k}_1 \mp \mathbf{k}_2 + \mathbf{k}_3$  corresponding to rephasing (−) and nonrephasing (+) signals, respectively. The IR pulses are generated using a continuum seeded dual-frequency two-stage optical parametric amplifier based on β-barium borate. The collinear signal and reference local oscillator are upconverted to the visible by sum-frequency generation in a wedged 5% MgO/LiNbO<sub>3</sub> crystal with a highly chirped 800 nm pulse that is derived from the uncompressed amplifier output before entrance into the compressor. The upconverted light is detected using a silicon CCD camera with 1340 horizontal pixels (Roper, PIXIS). The detection frequency,  $\omega_3$ , axis conjugate to  $t_3$  is obtained by the spectrometer, and

**TABLE 1:** Excitonic Hamiltonian Parameters and Experimental Frequencies<sup>a</sup>

Fit Parameters ( $\text{cm}^{-1}$ )										
$S_1$	$S_2$	$C_1$	$C_2$	$C_3$	$C_4$	$C_5$	$C_6$	$C_7$		
2020.38	2017.16	19.39	4.47	0.59	6.41	19.66	16.44	4.77		
Experimental Parameters										
mode	1	2	3	4	5	6	7	8	9	10
Hexane										
$\nu$ ( $\text{cm}^{-1}$ )	1981	1981	1983	1997	2014	2014	2024	2024	2044	2116
$\Delta\nu$ ( $\text{cm}^{-1}$ )			3.28		3.34	3.34			3.48	
$ \mu_l $ (a.u.)	0	0	0.659	0	1.0	1.0	0	0	0.813	0
Methanol										
$\nu$ ( $\text{cm}^{-1}$ )	1972	1979	1983	1998	2009	2012	2021	2027	2046	2116
$\Delta\nu$ ( $\text{cm}^{-1}$ )	7.7	10.95	9.3	10.46	10.70	10.56	10.1	8.9	5.2	
$ \mu_l $ (a.u.)	0.15	0.27	0.28	0.10	0.76	0.70	0.25	0.25	0.74	0

<sup>a</sup> Experimental Raman are taken from ref 47. The IR-active modes in hexane are determined by fitting the FTIR spectrum, and in methanol, all of the band frequencies are determined from fits to the FTIR spectrum.

the excitation axis,  $\omega_1$ , is obtained by Fourier transformation with respect to  $t_1$ . Recently, we have demonstrated how to obtain purely absorptive spectra,<sup>72</sup> correcting the spectral phase of the signal using the known spectral phase of the chirped pulse.<sup>73</sup> The time delay between the first and second pulses is scanned using independent pairs of ZnSe wedges. The maximum scanned delay is 10 ps, corresponding to an experimental Fourier transform resolution of  $3.3 \text{ cm}^{-1}$ .

**Simulation Methods.** Both 1D and 2D spectra have been successfully modeled using a vibrational exciton treatment, coupling local modes to yield the vibrational eigenstates. Using semiempirical transition dipole coupling between local mode units and a fixed vibrational anharmonicity of the resulting eigenstates, it is possible to use MD simulations to generate an ensemble of structures from which the 2D spectrum at  $t_2 = 0$  can be constructed from a sum of homogeneously broadened spectra. Although this approach does not provide information on the spectral diffusion of such an ensemble, it does aid in determining the inhomogeneous width as well as providing insight into the eigenstate energy landscape, including any pH, temperature, or solvent dependence. The most complete spectral simulation uses the dynamic frequency trajectory to compute the full multitime correlation function needed to predict the waiting-time-dependent 2DIR spectrum, capturing the spectral diffusion dynamics, and, in principle, vibrational redistribution and relaxation processes using, for example, a Redfield theory description of the dissipation. Spectral diffusion and chemical exchange have received recent attention in the literature.<sup>28–30,74–81</sup>

Rather than constructing an electric field map for the metal–carbonyl C≡O stretch, the model we have implemented simply imposes Gaussian-distributed local mode energy disorder, as is commonly done for electronic aggregates.<sup>37,55</sup> This model provides insight into the signatures of site disorder in a highly coupled multivibrational chromophore system. The Hamiltonian (eq 3),

$$H = \sum_{n=1}^{10} \varepsilon_n |n\rangle\langle n| + \sum_{n \neq m=1}^{10} J_{nm} |n\rangle\langle m| \quad (3)$$

describes the 10 carbonyl units using diagonal site energies  $\varepsilon_n$  and off-diagonal coupling  $J_{nm}$  terms. The assignment of the 10 sites is shown in Figure 1. The values of the matrix elements are determined by a genetic algorithm multivariable fit to the 10 experimental terminal carbonyl stretching frequencies. Based

on symmetry, the model has 7 coupling terms ( $C_1$ ... $C_7$ ) and two different site energies ( $S_1$  and  $S_2$ ) as follows,

$$H = \begin{bmatrix} S_1 & C_1 & C_1 & C_1 & C_1 & C_2 & C_2 & C_2 & C_2 & C_3 \\ C_1 & S_2 & C_4 & C_5 & C_4 & C_6 & C_6 & C_7 & C_7 & C_2 \\ C_1 & C_4 & S_2 & C_4 & C_5 & C_7 & C_6 & C_6 & C_7 & C_2 \\ C_1 & C_5 & C_4 & S_2 & C_4 & C_7 & C_7 & C_6 & C_6 & C_2 \\ C_1 & C_4 & C_5 & C_4 & S_2 & C_6 & C_7 & C_7 & C_6 & C_2 \\ C_2 & C_6 & C_7 & C_7 & C_6 & S_2 & C_4 & C_5 & C_4 & C_1 \\ C_2 & C_6 & C_6 & C_7 & C_7 & C_4 & S_2 & C_4 & C_5 & C_1 \\ C_2 & C_7 & C_6 & C_6 & C_7 & C_5 & C_4 & S_2 & C_4 & C_1 \\ C_2 & C_7 & C_7 & C_6 & C_6 & C_4 & C_5 & C_4 & S_2 & C_1 \\ C_3 & C_2 & C_2 & C_2 & C_2 & C_1 & C_1 & C_1 & C_1 & S_1 \end{bmatrix} \quad (4)$$

The fit is also constrained to reproduce the experimental IR transition strengths, including the IR inactivity of the six dark modes. Agreement was found by setting the local mode transition dipole moment of the axial carbonyls,  $\mu_{ax}$ , to have a magnitude 1.48 times that of the equatorial carbonyls  $\mu_{eq}$ . Since the model considers only the excitations on each local unit, there is no information regarding the vibrational anharmonicity or the associated excited state absorption. However, it is possible to include multiple excitations either explicitly or by using perturbation theory<sup>82</sup> or the nonlinear exciton equations.<sup>83</sup> Using the present model, the two-exciton manifold was calculated using a fixed anharmonicity of  $8 \text{ cm}^{-1}$ , allowing the 2D spectrum of DMDC to be simulated in the presence of site disorder. The experimental frequencies and the fit parameters for the one-exciton manifold are given in Table 1.

To simulate the hydrogen bonded solvent environment, we incorporate disorder into the model by allowing each diagonal site energy to vary according to a Gaussian random variable,  $\delta\omega_n$ , such that for each realization of the Hamiltonian, the  $n$ th site energy is  $\varepsilon_n = \varepsilon_n^{(0)} + \delta\omega_n$ , where  $\varepsilon_n^{(0)}$  corresponds to the perfectly ordered system. The  $\delta\omega_n$  are uncorrelated (unless specified otherwise) with zero mean, and we define the site inhomogeneous width  $\Delta\Omega_{in}$  to be the standard deviation of  $\delta\omega_n$ . Using eigenstate frequencies and transition moments determined from diagonalization of 5000 realizations with varying degrees of inhomogeneity, we found no correlation between the two. The eigenstate transition moments are calculated using the approximation that the local carbonyl units have their transition

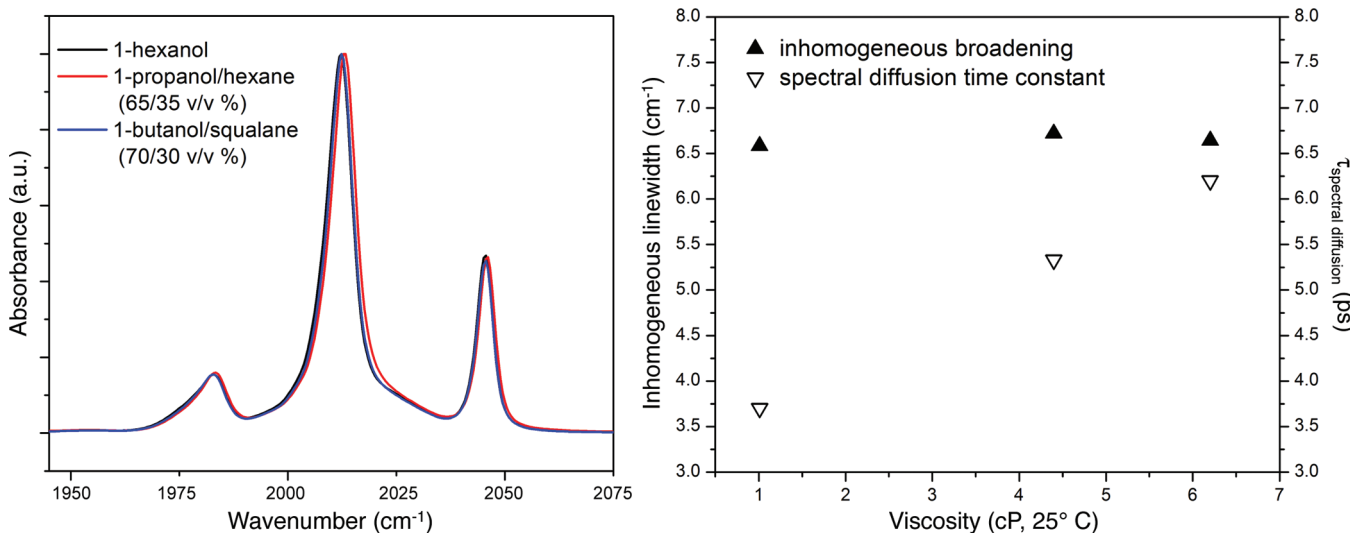


**Figure 2.** (left) FTIR spectra of DMDC in three solvent/solvent mixtures showing identical spectral lineshapes. (right) The inhomogeneous broadening contribution to the total FTIR line shape of the  $E_1$  modes as a function of solvent viscosity, as well as the spectral diffusion time constants of DMDC in each solvent system.

moments parallel to the CO bond axis; the eigenstate transition moments are obtained by the coordinate transformation defined by the Hamiltonian diagonalization. To compute the 1D spectrum, we used a Voigt profile, which takes as inputs the homogeneous (Lorentzian) and inhomogeneous (Gaussian) widths. The Voigt profile for each transition is then weighted by the square of the corresponding transition moment, and the sum of these is the linear spectrum. The Gaussian width for the Voigt profile corresponds to the standard deviation of the eigenstate frequency for each mode. We used an accurate analytical fit to a Voigt profile.<sup>84</sup>

In addition to the eigenstate frequencies, we also consider the eigenvectors to gain insight into the origin of the spectroscopic features exhibited by the model. As is common in analyses of J-aggregates and other excitonic systems, we consider the extent of delocalization via the participation ratio (PR).<sup>38,85</sup> In J-aggregates and in multichromophoric light-harvesting protein complexes, the excitons are often delocalized over many nanometers, and the size of the exciton decreases with disorder. By comparison, DMDC is a very small molecule, but the vibrational eigenstates are nevertheless delocalized over at least half of the carbonyl units. Thus, from the perspective of the number of participating monomers, the extent of delocalization is comparable to what is observed in, for example, LH2 complexes.<sup>42</sup> Like these large-scale electronic systems, as the site disorder is increased, the excitons become localized. Indeed, all of the trends we have noted thus far can be correlated to disorder-induced exciton localization.

Using each eigenvector  $\phi_n$ , we determine the degree of exciton localization resulting from site disorder. The participation ratio,  $P_n$ , given by eq 5 equals the number of local units (indexed by  $m$ ) that contribute to the resulting delocalized eigenstate  $\phi_n$ .<sup>38,60</sup>

$$P_n = \left[ \sum_{m=1}^{10} (\phi_n)_m^4 \right]^{-1} \quad (5)$$

For the present system,  $P_n$  ranges from 1 to 10. In addition to measuring the degree of localization, the participation ratio also allows us to discover any correlation between the localization tendency and the eigenstate frequency.

To illustrate the spectral signatures predicted by our exciton model for DMDC, we have simulated 2DIR spectra by including both the one- and two-exciton manifolds. Since our model treats only static disorder, we do not make any attempt to simulate the waiting time dependence of the 2D spectra. The 2D spectra were simulated using the one-exciton transitions and transition dipoles, and a quasi-harmonic ansatz for the two-exciton states. Overtone and combination band energies were computed as the sum of the one-exciton energies with a constant anharmonicity for all of the excited states of 8 cm<sup>-1</sup>. Harmonic oscillator scaling was assumed for all overtone transition dipole moments.

The transition dipole moment direction for a transition between a given one-exciton state  $a$  and a given two-exciton state  $ab$  was taken to be parallel to the transition dipole moment for excitation of the one-exciton state  $b$ . Combination band transition moments were scaled by the moduli of the constituent one-exciton transitions to account for their degree of allowdness. With the set of 10 one-exciton states and 55 two-exciton states as well as the transition dipole moments derived from the one-exciton Hamiltonian, we prepared multiple inputs for the SPECTRON package which we used to compute the 2D spectra.<sup>86</sup> The spectra were simulated using a constant exponential dephasing corresponding to a 2 cm<sup>-1</sup> homogeneous width, and the response function was evaluated using the sum-over-states method (the “CGF” option in SPECTRON 2.4.0).

### III. Experimental Results

**Linear and Nonlinear Spectroscopy.** Linear IR spectra are often used to extract dynamic information using analysis of the line width. This approach can often produce ambiguous dynamic results, in which multiple systems showing identical linear spectra exhibit different dynamics, such as orientational relaxation, population relaxation or spectral diffusion. This has been demonstrated clearly by Fayer and co-workers, for which four proposed water systems having identical linear IR spectra displayed different orientational relaxation times.<sup>87</sup> As shown here, three systems (two different binary mixtures and a pure long chain alcohol) displaying identical linear IR spectra are shown to have significantly different spectral diffusion times.

Three solvent or solvent mixtures, 1-hexanol, propanol/hexane (65/35% v/v) and butanol/squalane (70/30% v/v), have viscosi-

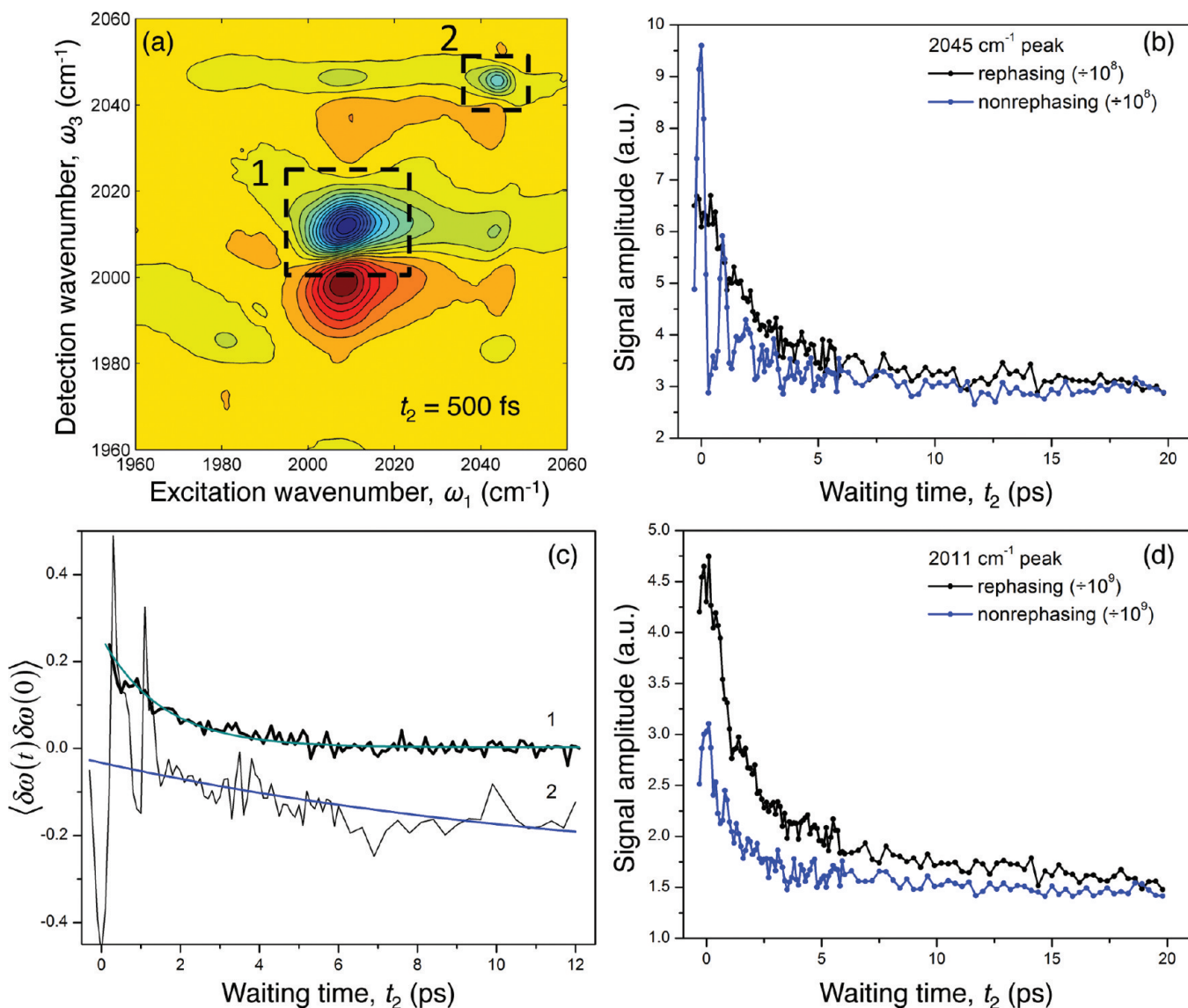


**Figure 3.** (a) 2DIR absorptive spectrum of DMDC in methanol at  $t_2 = 500$  fs with the  $E_1$  modes and high-frequency  $B_2$  mode highlighted. Rephasing and nonrephasing signals of the two modes (b and d), where the  $E_1$  modes have an enhanced rephasing signal at early times that is absent from the  $B_2$  modes rephasing signal. (c) The frequency–frequency correlation functions for these two modes display significantly different dynamics, where the  $B_2$  mode exhibits coherent oscillations but no pronounced spectral diffusion.

ties ranging from roughly 1 to 6 cP at 25 °C. In these solvents, DMDC displays identical linear IR spectra, shown in Figure 2 (left). Using the FFCF determined from the rephasing and nonrephasing 2DIR spectra (eq 1), the spectral diffusion time constants as well as the inhomogeneous contributions to the line shape were determined and are shown in Figure 2 (right). The spectral diffusion time constants, which range from roughly 3.5 to 6 ps, were found to depend on the solvent’s bulk viscosity. Despite the difference in the dynamical sampling of microenvironments, however, the inhomogeneous broadening of DMDC in these solvent mixtures is identical. The key observation from these data is that the time scale for spectral diffusion is independent of the magnitude of the microscopic fluctuations that produce the inhomogeneous width. The situation in the neat alcohols are markedly different, as shown below, where there is a pronounced correlation between inhomogeneous width and the time scale for spectral diffusion.

**Heterogeneous Dynamics of Coupled Vibrations in DMDC.** The four IR-active modes are highly delocalized vibrations that have been described by DFT calculations. The linear FTIR

spectrum of DMDC in methanol (Figure 1) shows significant broadening of the central and low-frequency peaks compared with DMDC in cyclohexane, but little broadening is seen on the high-frequency mode. This trend is common to the alcohol series shown below as well as several other polar solvents (not shown).

Figure 3a shows the absorptive spectrum of DMDC in methanol at a waiting time of 1 ps. Slices of the rephasing and nonrephasing spectra are shown in Figure 3b and d for the bands along the diagonal centered at 2045 and 2013 cm<sup>-1</sup>, respectively. Coherent oscillations are evident in the 2045 cm<sup>-1</sup> nonrephasing signal due to the coherence created between the low- and high-energy states in the first excited state manifold. These coherences have previously been described in detail for this system<sup>44</sup> as well as for  $\text{Co}_2(\text{CO})_8$ <sup>88</sup> and are the vibrational exciton analogues of similar coherences observed in electronic systems with excitonic coupling.<sup>57,58,89,90</sup> The slow dephasing is due to the narrow line width of the high-frequency band. Oscillations are not observed in the nonrephasing response for the central band. Such a feature would include contributions from a coherence

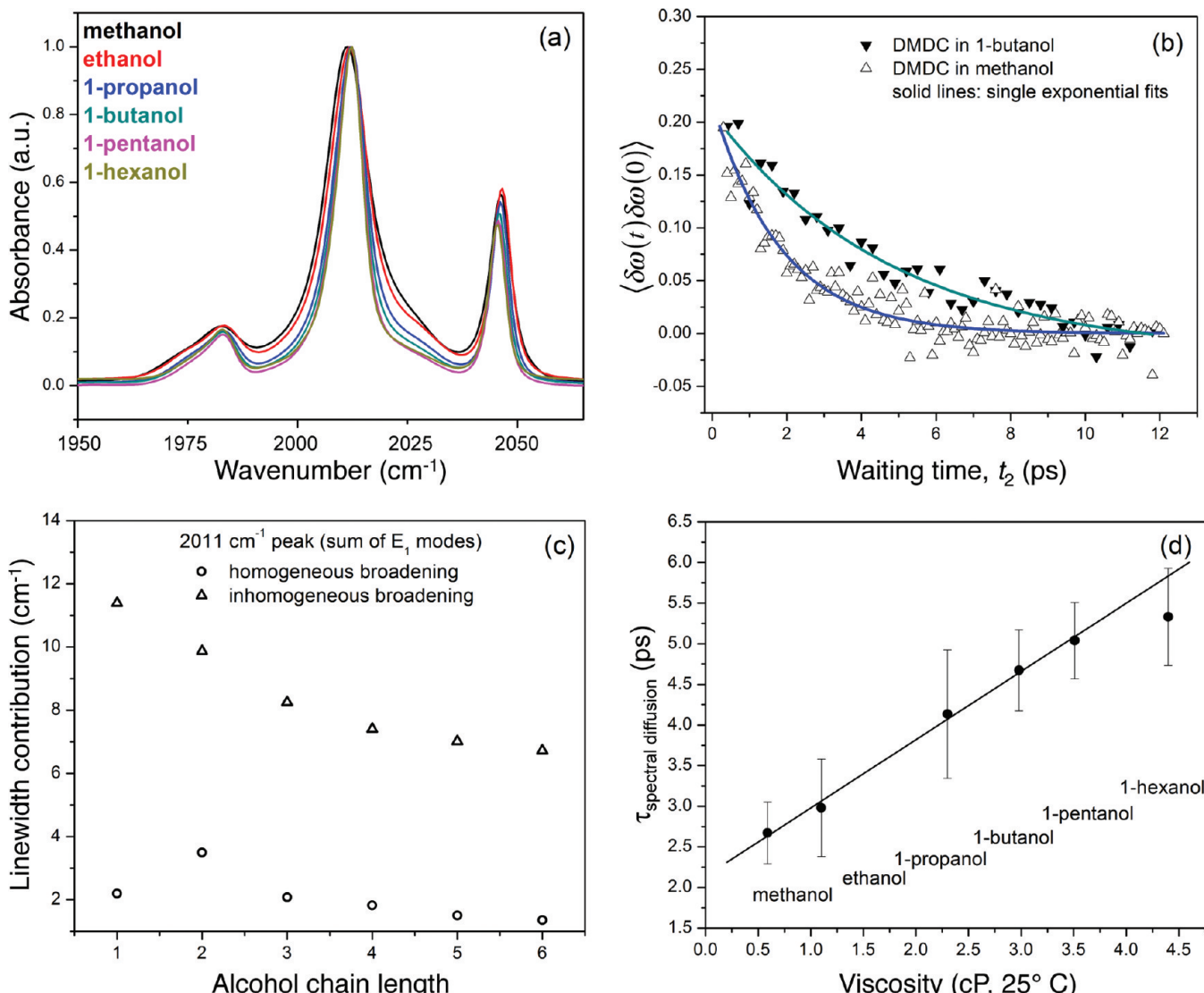


**Figure 4.** FTIR spectra of DMDC in a series of linear alcohols (a) and the corresponding homogeneous and inhomogeneous broadening of each system (c). (b) Example correlation functions of DMDC in methanol and 1-butanol. (d) Spectral diffusion time constants as a function of solvent viscosity.

between the broad central and low-energy bands, and their broad bandwidths lead to very rapid dephasing.

The FFCFs for the two bands are shown in Figure 3c. Although the large amplitude oscillations due to the intraband coherences obscure the FFCF at early times, the high frequency mode of DMDC in methanol shows little inhomogeneity and exhibits little to no loss of correlation, despite being in a polar solvent. Indeed, the fact that the coherences are so pronounced is a direct consequence of the comparable rephasing and nonrephasing signal amplitudes, a direct indication that the band is not significantly inhomogeneously broadened. Although there is additional information present in these low-frequency coherences, here, we focus on the spectral diffusion, where it can be seen that there is little to no memory loss for this vibrational mode, as well as line broadening that differs significantly from the central band. The difference in line broadening can also be seen in the line shape of the absorptive spectra, where the high-frequency mode has no peak elongation along the diagonal and a symmetric line shape at  $t_2 = 1$  ps. That two strongly coupled vibrational modes show different lineshapes suggests qualitatively distinct dynamics or differences in each band's response to solvation structure and dynamics.<sup>91</sup>

**Spectral Diffusion in Alcohol Series.** The spectral diffusion time scale for DMDC in a series of alcohol solvents, ranging from methanol to 1-hexanol, were determined using the method previously described. Figure 4a shows the FTIR spectra of DMDC in the series of alcohol solvents. The spectra become narrower with increased alkyl chain length. The central band center remains largely constant, but the high-frequency band shifts to the red with increased chain length. The presence of spectral amplitude at frequencies corresponding to IR-inactive modes also diminishes with increased chain length.

Figure 4b shows representative FFCFs for the solvents methanol and 1-butanol. The solid curves are single exponential fits to the data starting at  $t_2 = 100$  fs. It is evident from the data that the loss of frequency correlation in methanol is considerably more rapid than it is in 1-butanol. The early waiting time value of the correlation function corresponds to the fraction of the 1D line width that is due to inhomogeneous broadening. Although the early time value for methanol (0.15) is smaller than that of 1-butanol (0.2), the overall spectral width of methanol is greater than that of 1-butanol. Combining the two observations—methanol's broader spectrum and comparable inhomogeneous contribution—indicates that methanol induces

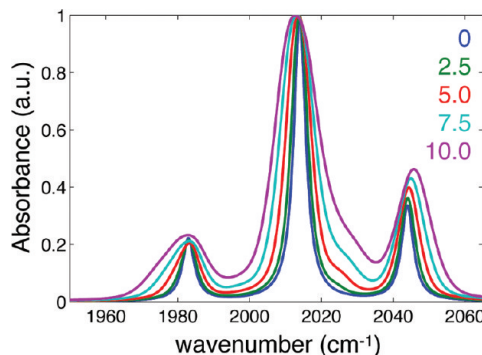


**Figure 5.** Simulated linear IR absorption spectrum of DMDC using the vibrational exciton Hamiltonian with site inhomogeneity  $\Delta\Omega_{in}$  varying from 0 to  $10.0 \text{ cm}^{-1}$ .

a broader inhomogeneous width. The full analysis described below is based on using a Voigt profile for the linear spectrum, and the two spectral width contributions are extracted using the method described by Kwak et al.<sup>1</sup>

Figure 4c shows the extracted homogeneous and inhomogeneous widths of the central band of DMDC in the alcohol series. The inhomogeneous widths decrease monotonically from  $11 \text{ cm}^{-1}$  for methanol to  $7 \text{ cm}^{-1}$  for 1-hexanol. Except for a slight difference in the case of ethanol, the homogeneous widths likewise decrease with increasing alcohol chain length, although the overall variation is less than  $1 \text{ cm}^{-1}$ . It is key to note here that this band is composed of two degenerate modes, and according to the model presented below, these states are split by site disorder. Thus, the extracted width of the central band is actually the combined widths of two bands. From the model, it is possible to deduce the width of the combined band, and this analysis is presented in the discussion.

Figure 4d shows the spectral diffusion time constants extracted using eq 2, as was also done for the case of the solvent mixtures. The spectral diffusion times depend monotonically on the solvent viscosity, ranging from  $2.67 \text{ ps}$  in methanol to  $5.33 \text{ ps}$  in 1-hexanol. There is a linear dependence of spectral diffusion time on solvent viscosity from methanol to 1-pentanol, with some deviation for the longest chain solvent 1-hexanol.

#### IV. Simulation Results

Analysis of the vibrational exciton model is broken into two parts: the first describes general aspects of the eigenstate distributions and the spectral lineshapes as a function of  $\Delta\Omega_{in}$ ; the second compares the model to the measured data described above.

Figure 5 shows several spectra generated using the model exciton Hamiltonian with varying values of the site disorder frequency width  $\Delta\Omega_{in}$ . In addition to the initial fit to the known experimental IR and Raman frequencies and IR transition moments, there are no further adjustable parameters. The model spectra reproduce the experimental 1D spectra remarkably well. In this section, we analyze the model’s results to deduce a molecular interpretation for the origin of the spectral changes.

For this simplified model of the vibrational Hamiltonian, we have considered only the effect of diagonal disorder, since hydrogen bonding between the alcohol solvent and the carbonyl units is a local interaction. It should be noted, however, that the site energies and the coupling matrix elements are not independent parameters, and future studies will need to include disorder in the full Hamiltonian. To sample a range of broadening that resembled the experiment,  $\Delta\Omega_{in}$  ranged from 0 to  $25 \text{ cm}^{-1}$ , and for each value of the local site inhomogeneity,

5000 realizations were evaluated. The resulting eigenvalues are enumerated from 1 to 10 in increasing energy and are identified as either “IR”- or “Raman”-active according to their zero-disorder activity; hence, modes 3, 5, 6, and 9 are the “IR modes”, whereas 1, 2, 4, 7, 8, and 10 are the “Raman modes.” The zero-disorder frequencies are shown in Table 1.

Figure 6a shows the average transition frequencies for each eigenstate as a function of the site disorder frequency width,  $\Delta\Omega_{in}$ . It is immediately clear that the two E modes—degenerate in the absence of disorder—split with increasing site disorder. Both B modes (3 and 9) increase in frequency initially, and then mode 3 starts to decrease when the site disorder becomes comparable to the large coupling terms in the Hamiltonian near  $\Delta\Omega_{in} = 15 \text{ cm}^{-1}$ . For the Raman modes, a similar symmetry breaking is also clear: modes 1 and 2 are initially degenerate but become split by the increased disorder and shift to lower frequency. A similar trend is evident for modes 8 and 9, although they shift to higher frequency as they split. Mode 10 is not shown in these figures, since it never acquires appreciable IR oscillator strength for the range of disorder considered here.

Along with the changes in the average eigenstate frequencies, there is also a clear trend in the oscillator strengths. In general, all of the IR-active modes lose oscillator strength, whereas all of the Raman modes gain oscillator strength. Figure 6b shows the IR and Raman mode transition moments as a function of  $\Delta\Omega_{in}$ . Among the IR modes, the principle difference is the rate at which the modes lose oscillator strength. Compared to the rather gradual decrease seen in the higher-frequency modes (5, 6 and 9), mode 3 loses almost half of its oscillator strength by  $\Delta\Omega_{in} = 10 \text{ cm}^{-1}$ . This finding is consistent with our experimental observations and explains the much weaker diagonal and cross peaks seen in the 2D spectra for the lowest frequency band. The gradual increase in oscillator strength above  $\Delta\Omega_{in} \approx 15 \text{ cm}^{-1}$  is likely due to the limited applicability of including only site disorder in our model. The Raman modes gain IR oscillator strength with increased disorder, with the lower frequency modes (1 and 2) growing at a somewhat faster rate than the higher frequency modes.

Figure 6c shows the mean participation ratio (eq 5) as a function of the site energy inhomogeneity. The results clearly indicate that exciton localization is induced by disorder. All of the modes exhibit localization, with the more rapid and pronounced change seen in mode 3, which localizes by two carbonyl units with only about  $3 \text{ cm}^{-1}$  of disorder. The localization of mode 3 corresponds well to the loss of oscillator strength seen in Figure 6b. Modes 5 and 9 show the smallest degree of localization, whereas mode 6 contracts by about 20% with about  $8 \text{ cm}^{-1}$  of site disorder. The Raman modes also show varying degrees of localization, with the single exception of mode 4, which actually becomes more delocalized with increased disorder. Modes 7 and 8 abruptly collapse with the slightest degree of disorder, reflecting their high symmetry. Modes 1 and 2 remain relatively delocalized, which again correlates with their rapid onset of oscillator strength.

In addition to the average properties shown in Figure 6, we also examine the frequency widths of the eigenstates. For each value of  $\Delta\Omega_{in}$ , we take the standard deviation of each resulting eigenstate distribution as a measure of its inhomogeneous width. It is well-known from molecular aggregates that in coupled systems, the eigenstate width is narrower than the site width.<sup>39</sup> This exchange narrowing is a result of averaging over the site energy fluctuations.

Figure 7 shows the vibrational exciton inhomogeneous width together with the correlation with the inverse of the participation

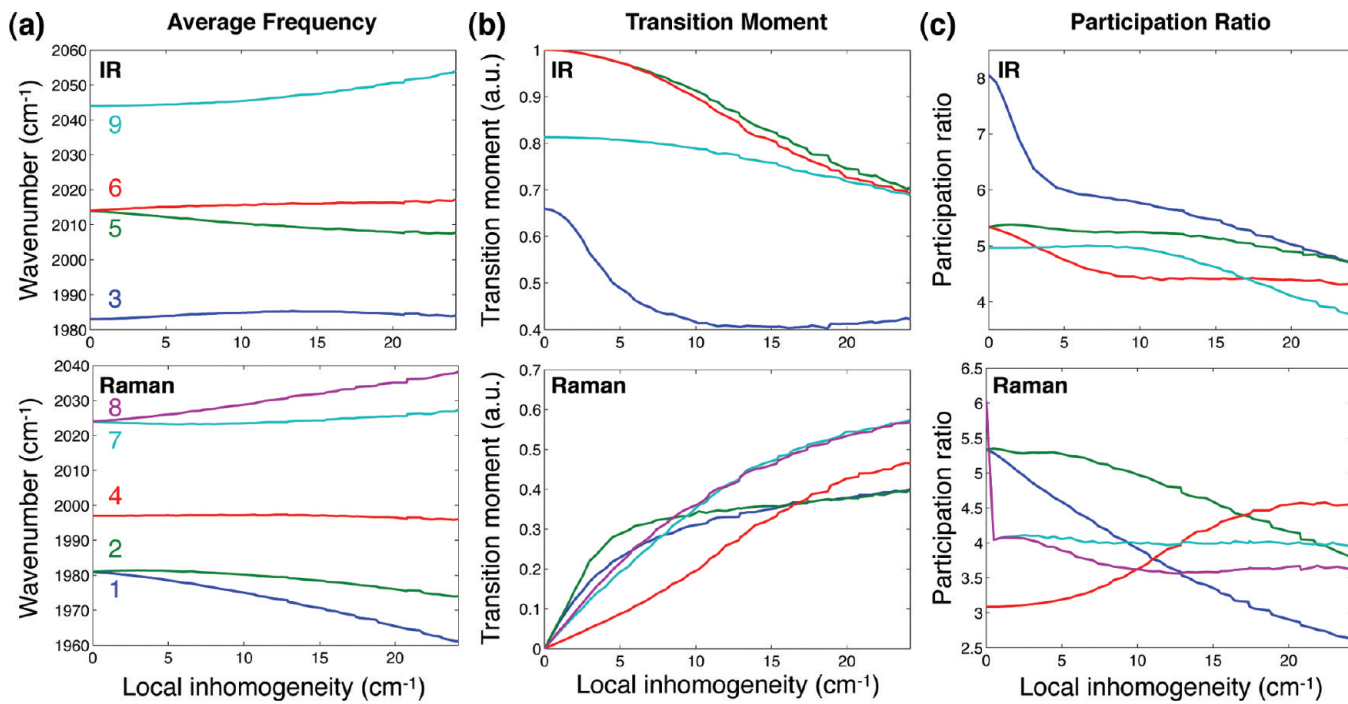


**Figure 6.** Eigenstate properties (a) average frequency, (b) transition moment, and (c) participation ratio (PR) for (top) the four IR active modes (modes 3, 5, 6 and 9) and (bottom) the five Raman modes (modes 1, 2, 4, 7 and 8) that acquire appreciable IR activity due to the site disorder.

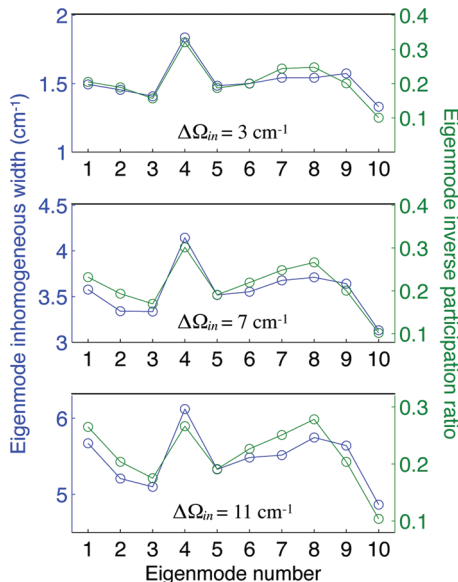


**Figure 7.** Correlation between the inhomogeneous widths of each ensemble of eigenmode frequencies (left axis) and the eigenmode inverse participation ratio (right axis) for three representative values of the local site inhomogeneity, 3, 7, and 11 cm<sup>-1</sup> (top to bottom).

ratio. At three selected values of  $\Delta\Omega_{in}$ , we find that the eigenstate width tracks the participation ratio. Since the participation ratio is the number of local mode units over which the exciton is delocalized, a larger inverse participation ratio indicates a higher degree of localization. Thus, the data show that the inhomogeneous width correlates with the degree of exciton localization, consistent with many studies of exchange narrowing in molecular aggregates. Note that in all cases, the eigenstate widths are narrower than the site widths. The relationship between site and exciton energy disorder allows us to associate a site energy distribution with the inhomogeneous widths determined from the FFCFs (Figure 4c). Since the inhomogeneous and homogeneous broadening parameters shown

in Figure 4c are for the whole central band, where the two degenerate modes are split by the site disorder and thus increase the band's overall width, our estimate of the local site energy width is only an upper bound. Nevertheless, we can estimate the site energy full width at half-maximum to be 31.5 cm<sup>-1</sup> ( $\text{fwhm} = 2\Delta\Omega_{in}(2 \ln 2)^{1/2}$ ), for the case of methanol, which is substantially greater than the 11.7 cm<sup>-1</sup> inhomogeneous width. For the case of 1-hexanol, where the inhomogeneous width was measured to be 7 cm<sup>-1</sup>, comparison with the model gives a site energy fwhm of 18.5 cm<sup>-1</sup>.

Another informative measure that has been considered in molecular aggregates is the correlation between the participation ratio and the eigenstate frequency.<sup>38</sup> Figure 8a–b shows a summary of the results for  $\Delta\Omega_{in} = 4.5$  cm<sup>-1</sup>. This figure combines several of the considerations above—frequency, PR, and inhomogeneous width—and illustrates that for the low-frequency modes, there is generally a positive correlation between frequency and PR (i.e., delocalization), whereas for the highest frequency mode, the correlation is negative. In the middle of the band, the frequency and PR values are only weakly correlated. The results also indicate the lack of a clear trend in the absolute delocalization across the band, which differs from the trend in molecular aggregates, where more delocalization has been observed in the band center relative to the band edges. When the degree of disorder is increased further, however, the expected trend is observed (Figure 8c): the delocalization is greater in the center of the band relative to that in the wings, with the exception of mode 10, whose high symmetry resists localization.

In addition to the 1D spectrum, the 2D absorptive spectrum of DMDC was simulated as described in section II. These simulations demonstrate the characteristic spectral signatures of the general trends we have described above. Figure 9 shows the 2D spectrum of DMDC calculated for  $\Delta\Omega_m = 0, 3$ , and 7 cm<sup>-1</sup>, with a fixed homogeneous width of 2 cm<sup>-1</sup>. Figure 9a shows the spectrum with no site disorder, and the simulation, which agrees well with our previous experimental results,<sup>92</sup>

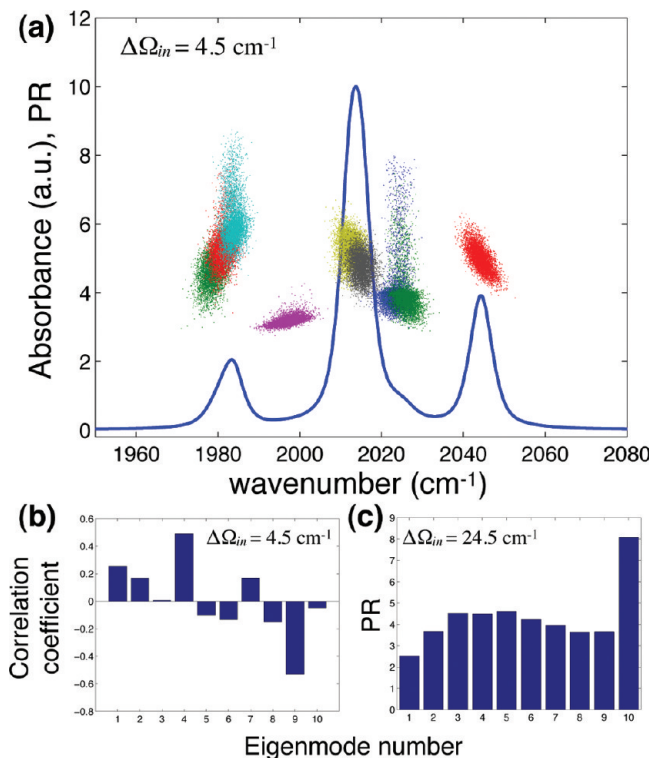


**Figure 8.** (a) Spectrum and ensemble of PR values plotted as a function of individual mode frequency. Each cluster of colored dots corresponds to a different eigenmode. (b) PR-frequency correlation coefficient of each eigenmode, showing generally positive correlation for the low-frequency modes and negative correlation for the high-frequency modes. (c) For the case of large site disorder, the PR-versus-mode number exhibits the trend that delocalization is greatest near the center of the spectrum, except for the highly symmetric mode 10.

clearly displays no inhomogeneous broadening evident from the largely symmetric peak shapes. Some slants of the cross and diagonal peaks are evident and are due to well-known Liouville path differences between rephasing and nonrephasing sequences previously observed in other metal carbonyl systems.<sup>64,65</sup> Upon the addition of  $3 \text{ cm}^{-1}$  of site disorder, the spectrum becomes noticeably broader, and the peak shapes begin to elongate along the diagonal (Figure 9b). Finally, with  $7 \text{ cm}^{-1}$  of site disorder, the spectrum shows several dark transitions and significant spectral broadening (Figure 9c).

**Site Disorder Correlation.** So far, we have considered only uncorrelated site disorder. Since recent simulation and experi-

ment shows that hydrogen bond switching occurs largely by rapid angular jumps,<sup>43,93,94</sup> it is very likely that there will be site energy correlations as a hydroxyl hydrogen bond breaks from one carbonyl and forms with an adjacent carbonyl. Such a scenario could lead to a negative frequency correlation, since the site of the broken bond would experience a blue shift accompanied by a red shift on the site gaining the hydrogen bond. Very recently, hydrogen bond rearrangement around an anionic solute has been found to involve cooperative motion reminiscent of the Grotthuss mechanism for proton transport in liquid water.<sup>93,94</sup> Understanding the collective hydrogen bond network rearrangement is a general goal of condensed phase dynamics, and molecules such as DMDC offer an attractive probe of these coordinated fluctuations.

Though it is difficult a priori to devise a site energy correlation scheme that is physically correct, we nevertheless consider what the effect of positive or negative correlation would be. We use the distances  $\Delta r_{ij}$  between pairs of oxygen atoms  $i$  and  $j$  to construct a covariance matrix  $\mathbf{M}_{ij}$  according to the following scheme

$$\mathbf{M}_{ij} = \delta_{ij} + \alpha \frac{(1 - \delta_{ij})}{\Delta r_{ij}^4} \quad (6)$$

where the amplitudes of the off diagonal elements ( $1 - \delta_{ij}$ ) are proportional to the inverse fourth power of the distance, which preferentially correlates those sites that are closest to each other. There is an overall scaling factor,  $\alpha$ . Multiplying the set of uncorrelated site energies by the Cholesky decomposition of  $\mathbf{M}_{ij}$  produces Gaussian randomly distributed site energies with intersite correlation given by the covariance matrix elements.<sup>95</sup> The sign and amplitude of the correlations are set by the parameter  $\alpha$ . In our implementation, we first normalize the off-diagonal matrix elements to the maximum value and then multiply all the values by  $\alpha$  before adding the diagonal elements (all of which are equal to unity). This normalization ensures that the largest correlation coefficient is equal to  $\alpha$ .

Figure 10 shows a summary of  $|\alpha| = 0.15$  comparing positive and negative correlation. The sign of the correlation appears to have little effect on the values of PR, mean frequency, and the transition moments. On the other hand, the degree of exchange narrowing is more pronounced for the negatively correlated case. Indeed, negative correlation reduces the inhomogeneous width by roughly a factor of 2 relative to the case of positive correlation.

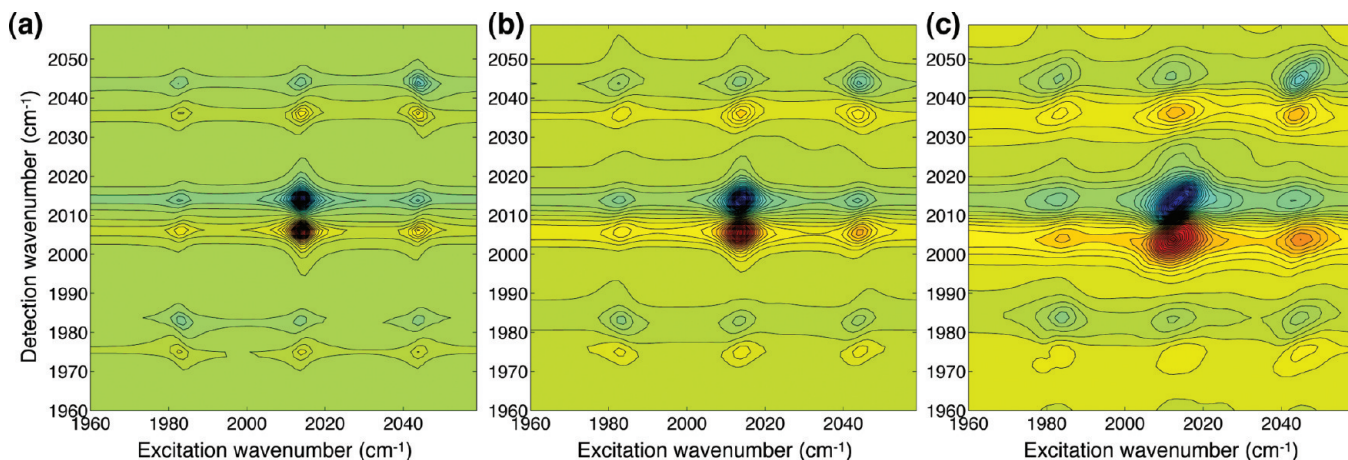


**Figure 9.** Simulated 2DIR spectra ( $t_2 = 0$ ) of DMDC computed using the 10 one-exciton and 55 two-exciton states with local site disorder  $\Delta\Omega_{in} = 0$  (a),  $3$  (b), and  $7 \text{ cm}^{-1}$  (c).

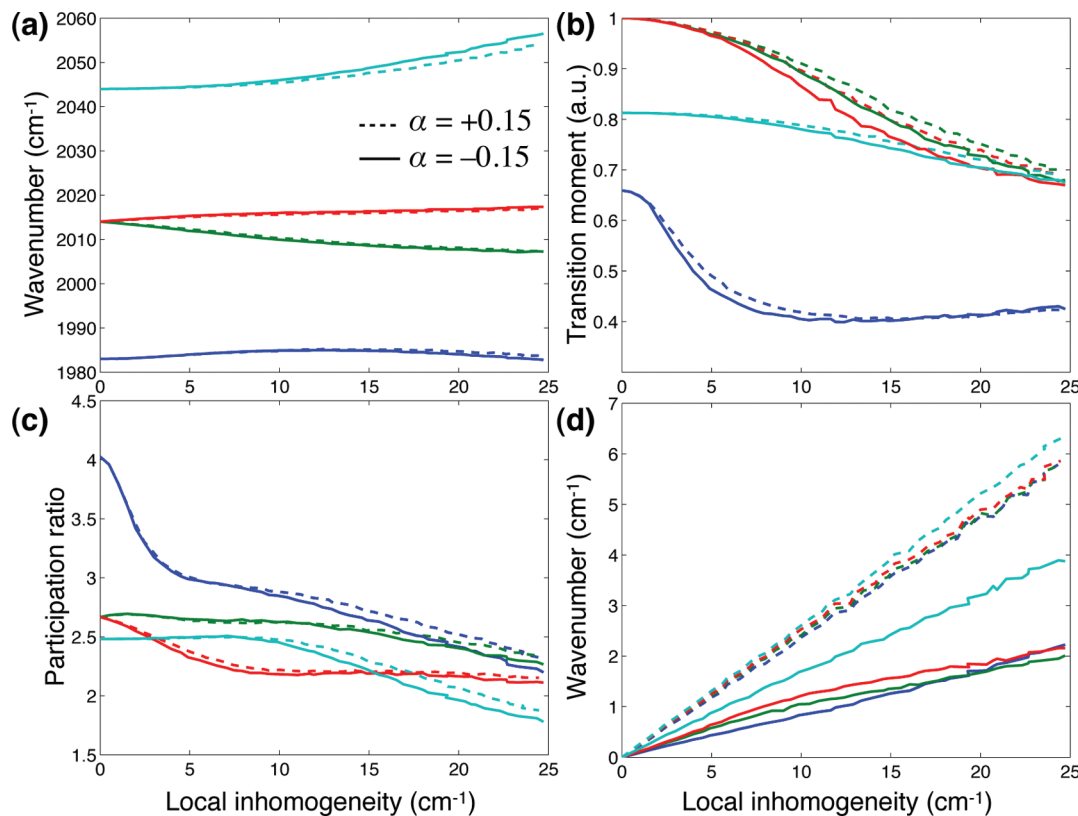


**Figure 10.** Simulations including correlation between sites—solid traces correspond to  $\alpha = -0.15$ , and dashed traces to  $\alpha = +0.15$ —of (a) average mode frequency, (b) average transition moment, (c) average PR, and (d) the standard deviation of the eigenmode ensemble. Only the IR-active modes are shown in this figure using the same color coding as in Figure 6.

Since the spectroscopy probes the eigenstates, it is instructive to consider their properties. One relationship among the eigenstates is their mutual eigenenergy correlation. It has been shown experimentally and through simulation that the extent and sign of correlation of two different exciton states is evident in the tilt of the cross peak connecting the two states.<sup>65</sup> For a fixed value of the site inhomogeneity ( $\Delta\Omega_{in} = 6 \text{ cm}^{-1}$ ), we evaluate the matrix of correlation coefficients for both positive and negative site disorder correlation. Figure 11 shows the predicted spectra with the superposed PR together with the matrix of eigenvalue correlation coefficients. The essential observation is that the correlation between the central band (modes 5 and 6) with the strong high-frequency band (mode 9) is positive with positive intersite correlation, whereas the bands are negatively correlated with negative intersite correlation.

This prediction can, in principle, be compared with the experiment, despite the fact that the presence of coherences complicates the clean extraction of the cross-peak tilt, since it is well-known that coherent beating leads to cross-peak tilt oscillations.<sup>96,97</sup> The simulated 2D absorptive spectra with intersite correlation are shown in Figure 12, using  $\alpha = \pm 0.15$ . Due to the inherent tilt of the cross peak between mode 9 and modes 5 and 6, the predicted frequency cross-correlation is not evident in the simulated 2D spectra. Instead, a clear difference is observed in the degree of frequency correlation of the excited state absorption from modes 5 and 6, shown in the boxed region and zoomed. The spectrum simulated with positive correlation shows a more pronounced peak tilt in the spectrum parallel to the diagonal, whereas the spectrum simulated with negative correlation shows a reduced tilt angle as well as the narrower width expected from the simulated 1D spectra (Figure 11).

To highlight the differences, we found the peak maximum along  $\omega_3$  for various values of  $\omega_1$  using the center of a Gaussian

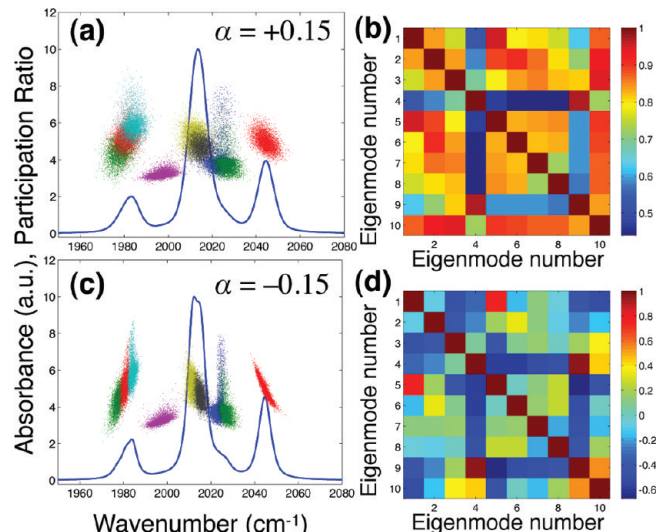


**Figure 11.** Spectra and eigenmode PR values for (a) positive and (c) negative site correlation. Maps of the correlation coefficients (indicated in the color bars) of eigenmode frequencies for (b) positive and (d) negative site correlation.

fit. Figure 13a shows the  $\omega_3$  maxima for the ground state bleach and stimulated emission band, and Figure 13b shows the  $\omega_3$  maxima for the excited state absorption bands. Negative correlation leads to both a narrower inhomogeneous width ( $\sim 7$  vs  $\sim 11 \text{ cm}^{-1}$  for positive correlation), as indicated by the region where the frequencies are correlated, and the degree of correlation is also reduced as indicated by the smaller slope of the correlation. This effect is most pronounced for the excited state absorption band, in which the ratio of the slopes is roughly 2. Although it is difficult to extract the contribution due to intersite

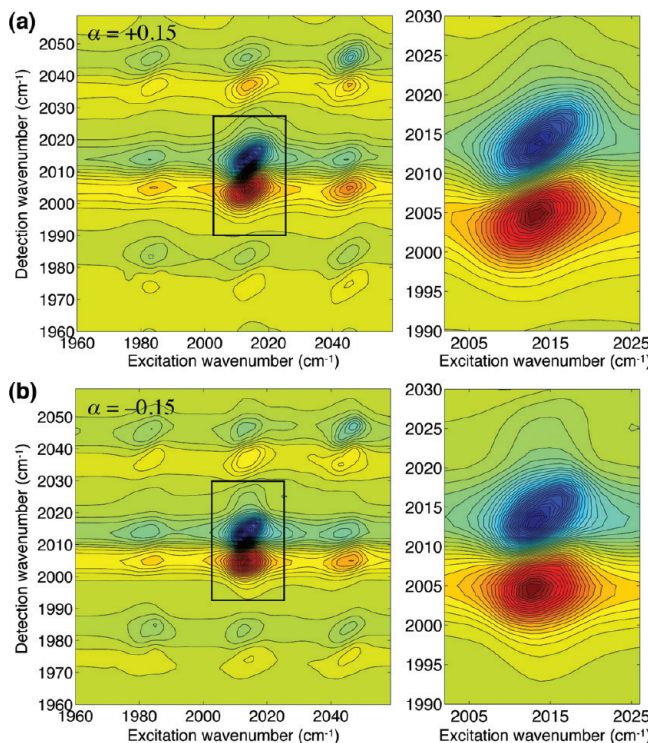


**Figure 12.** Simulated 2DIR spectra with positive ( $\alpha = 0.15$ ) (a) and negative ( $\alpha = -0.15$ ) (b) site energy correlation. The right panels are zooms of the central band involving modes 5 and 6. The site inhomogeneity is set at  $6 \text{ cm}^{-1}$ .

frequency correlation from measured 2D spectra, it is encouraging that such correlations do influence the observed 2D line shapes.

## V. Discussion

**Spectral Diffusion in the Alcohol Series.** The frequency correlation time is found to have a monotonic dependence on the solvent viscosity, where methanol shows the fastest spectral diffusion time scales, and 1-hexanol, the slowest. The dependence of spectral diffusion on solvent viscosity can be explained by the fluctuation rate, in which motional diffusion throughout the first solvation shell is significantly hindered as the chain length is increased. The slowing of molecular motions leads to prolonged hydrogen bond interactions, and transition frequencies that are a function of these interactions stay correlated for longer periods of time. In the case of localized vibrations, spectral diffusion has been reliably predicted using simple molecular diffusion models, such as the Stokes–Einstein relation to determine the diffusion constant of the solvent.<sup>98</sup> This relationship appears to break down when considering delocalized modes, where molecular diffusion models predict significantly longer spectral diffusion times. The spectral diffusion time scales predicted by the molecular diffusion model range from 1 ps in methanol to 27 ps in 1-hexanol. This disagreement suggests that the spectral diffusion of DMDC (and perhaps other delocalized systems) in alcohol solvents does not strongly depend on large-scale solvent diffusion within or throughout the first solvation shell. However, the energetics and dynamics of the system could be affected by the global structure in the liquid and local inhomogeneities that such a network could induce.

As seen in the FTIR spectra of DMDC in the alcohol series (Figure 4a), methanol leads to the broadest spectrum, with additional contributions from otherwise IR inactive modes. Therefore, the broadening seen in the IR spectrum of DMDC

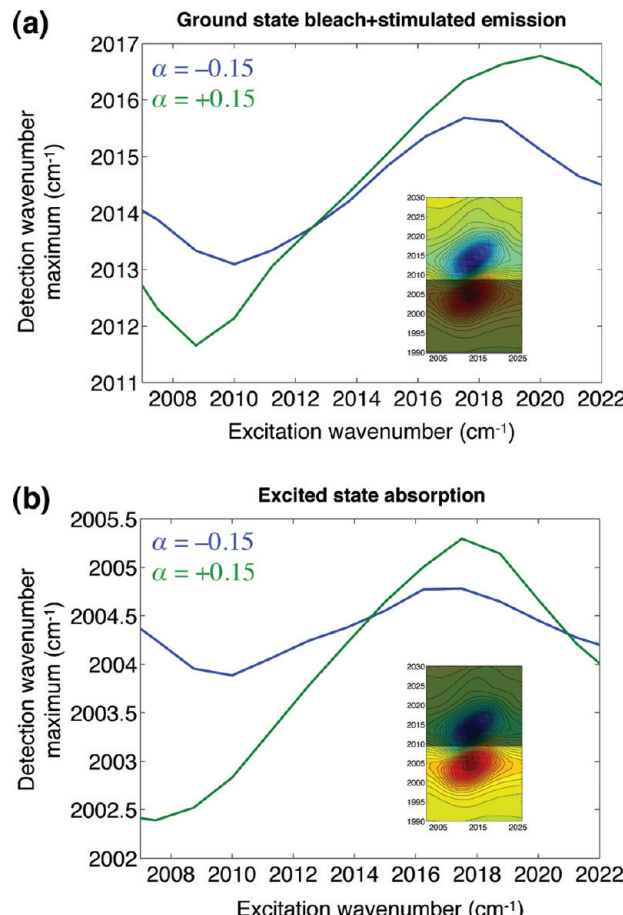


**Figure 13.** Plots of the correlation between  $\omega_3$  emission maximum versus excitation frequency,  $\omega_1$ , for (a) the peak due to ground state bleach and stimulated emission and (b) the peak due to excited state absorption. For each band, the case of negative (blue) and positive (green) site energy correlation are shown.

in methanol is not simply due to a distribution of transition frequencies but, instead, has contributions from dark vibrational modes as well as degeneracy splitting. As the chain length is increased, the fluctuations of the solvent are impeded, and the extent of symmetry breaking is reduced. As the solvation environment is limited in its configurations, the spectral broadening is reduced. The smaller magnitude fluctuations also lead to less dynamic exciton localization. Thus, in 1-hexanol, the spectral features are relatively narrow and there are only small contributions from dark modes.

**High Frequency Mode.** Above, we reported that the inhomogeneity in the transition frequency of the  $2045 \text{ cm}^{-1}$  mode does not follow the trend that is seen in the other vibrational modes. The 1D spectrum shows that the broadening of this mode throughout the alcohol series remains essentially constant, whereas other modes display greater inhomogeneous broadening in the more polar, short-chain alcohols. Even in methanol, the most polar alcohol solvent used in this study, the correlation function extracted from the 2D spectrum suggests that the vibrational mode is almost completely homogeneously broadened and shows no spectral diffusion. The simulated absorptive spectrum of DMDC with site disorder shows distinct peak elongation along the diagonal for the high frequency peak (Figure 9), whereas the experimental absorptive spectrum of DMDC in methanol shows no peak elongation (Figure 3a), even at early times. The vibrational exciton model used in this work accurately predicts the blue shift of this vibrational mode when

site disorder is added but does not accurately reproduce its resistance to inhomogeneous broadening.

The vibrational exciton model used in this work assumes a Gaussian distribution of transition frequencies to induce site disorder. This simple model of site disorder accurately predicts many aspects of the 1D and 2D spectrum of DMDC in alcohol solvents, but the Gaussian model for transition frequency distribution is not sufficient for predicting the full 1D and 2D spectrum of DMDC in systems that cause a large degree of inhomogeneous broadening. The simplest expression for the line shape function uses the second order cumulant approximation, but recent work has suggested that non-Gaussian dynamics could influence the line shape of systems that interact strongly with their environment.<sup>91,99</sup> Furthermore, it has been demonstrated that non-Gaussian fluctuations can lead to dissimilar dynamics of coupled vibrational modes.<sup>99–101</sup>

1D and 2D IR lineshapes and line shape dynamics that are not accurately reproduced by Gaussian frequency fluctuations have been observed in hydrogen bonded environments, including the amide I transition in aqueous environments<sup>99</sup> and the OH transition of water in acetonitrile.<sup>91</sup> In the case of the strongly coupled vibrational modes of the symmetric and asymmetric OH stretches of water in acetonitrile, the two coupled vibrational modes display significantly different frequency dynamics. This effect was attributed to non-Gaussian statistics, giving rise to nonzero odd-order correlation functions, which vanish in the case of Gaussian statistics. The non-Gaussian character of the hydrogen bond distance along the N–H coordinate leads to non-Gaussian frequency fluctuations, which are strongly dependent on the hydrogen bond coordinate.

The apparent non-Gaussian characteristic of the hydrogen bond dynamics occurring in DMDC in alcohol solvents could be the result of a non-Gaussian distribution of hydrogen bond distances between the carbonyl groups of DMDC and the hydroxyl groups of the alcohol solvent. Similar to the coupled vibrations of the water OH stretch in the H<sub>2</sub>O/CH<sub>3</sub>CN system, the strongly coupled vibrational modes of DMDC exhibit significantly different dynamics, as seen through the frequency–frequency correlation function. By coupling the current exciton model with MD simulations, it will be possible to gain an atomistic view of the hydrogen bonding environment, including the distribution of hydrogen bond distances and angles. Whether non-Gaussian dynamics alone account for the large difference in line shape and dynamics of the vibrational modes of DMDC will be the subject of a future study.

**Nature of the Solvation Environment.** Although it is established that alcohols contain some amount of polar/nonpolar structural segregation, the picture of alcohol structure that emerges from several simulation and experimental studies is that of a relatively well mixed hydrophobic and hydrophilic medium.<sup>33,35,36,102</sup> The smaller and more flexible solvents are able to present the DMDC probe with a larger range of hydrogen bonding configurations, whereas the lower viscosity facilitates rapid fluctuations of this solvation shell. On the other hand, the longer-chain alcohols are sterically confined while exhibiting slower dynamics.

Excellent agreement between experiment and the vibrational exciton Hamiltonian with site disorder enables us to deduce a molecular picture of the solvation environment probed by the 1D and waiting-time-dependent 2DIR spectra reported above. Since DMDC is amphiphilic, both the 1D and 2D spectra contain both polar and nonpolar contributions, and it remains to be determined how the single site disorder parameter maps to the distinct solvation environments. If the DMDC solute were

present only in a polar environment with a nearly complete hydrogen bonded solvation shell, we would conclude that as the solvent chain length is increased, the magnitude of the energetic fluctuations would decrease due to the increased stiffness of the more viscous solvents. From the spectral diffusion time scale, we would also conclude that the rate at which the frequencies are sampled decreases. Both conclusions are consistent with the 2DIR data, and the modeling explains why the frequencies shift with increased disorder and why the Raman modes become bright in the infrared.

Since the first implementations of liquid-phase X-ray scattering, there has been interest in the structure of alcohols.<sup>103,104</sup> It is known that these liquids are structurally heterogeneous due to the need to balance hydroxyl hydrogen bonding and the hydrophobicity of the alkyl tails.<sup>105</sup> The result of these competing interactions is that linear alcohols adopt structures that to some degree segregate polar and nonpolar regions. Simulation and experimental studies have concluded that linear alcohols form aggregates of varying size corresponding to the alkyl chain length. A recent simulation study characterized the aggregate topology and found that from methanol to 1-octanol, the aggregates were largely linear or branched, with only a small fraction (<5%) in ring or lasso aggregates.<sup>33</sup> These authors also found the aggregate size to range from 1 to 5 nm throughout the series, with a trend toward larger diameter with increased alkyl chain length. The shift in the aggregate size distribution was found to be due largely to the increased size of the molecules rather than to the number of molecules in the aggregates. In fact, there was little variation in number density of the aggregates from methanol to 1-octanol, with roughly 4 molecules in linear aggregates and 15 molecules in branched aggregates (these values refer to maxima in the number density distributions). Thus, despite the existence of aggregates, which certainly are responsible for rich structure and dynamics in alcohols, the solvent is nevertheless largely a well-mixed binary mixture of hydrophobic and hydrophilic components. We anticipate the framework described here to be instrumental in developing extended vibrational chromophores as probes of complex solvation environments such as alcohols, polymers, and lipids.

## VI. Conclusion and Outlook

We have reconsidered the delocalized coupled complex of carbonyl oscillators in Mn<sub>2</sub>(CO)<sub>10</sub> as a vibrational aggregate and have shown experimental and modeling results that indicate the complex can serve as a probe of large-scale hydrogen bonding solvation networks. Using an alcohol series to vary both the inhomogeneous broadening and the time scale for spectral diffusion, we find that DMDC is sensitive to local structure and dynamics in strongly interacting environments. With the alcohol series as a calibration, we identified several solvent systems consisting of pure solvents and solvent mixtures that result in identical linear FTIR spectra and inhomogeneous widths, but whose spectral diffusion time scales reflect the variation in solvent viscosity. To develop a predictive yet intuitive picture of the coupled vibrations in DMDC, we used an exciton model parametrized to reproduce the experimental transition frequencies and IR transition moments. With the simple addition of Gaussian site energy disorder, we found striking reproduction of several solvent-dependent spectral features observed experimentally. These included trends in the line shape, reflecting the manifestation of pronounced exchange narrowing, and the appearance of IR inactive modes due to the disorder induced symmetry breaking.

Correlations between sites also leads to testable signatures in the 2DIR spectrum in the form of correlated or anticorrelated cross-peaks reflected in the tilts relative to the diagonal. Despite the many successes, the model fails to reproduce the lack of inhomogeneous broadening of the highest-frequency IR mode, suggesting that qualitatively distinct dynamics or system–bath interactions influence that mode’s transition energy. Beyond the 1D spectra and analysis of the one-exciton manifold, we computed the two-exciton manifold and used these states to simulate 2DIR spectra. These simulations largely confirm the observations of the analysis based only on the one-exciton manifold. The 2D simulations also demonstrated an effect of intersite frequency correlation on the 2D peak shapes, where negative site correlation was found to reduce the overall frequency correlation, particularly that probed in the excited state absorption band. This initial investigation prepares the groundwork for further computational studies using dynamical simulations in the place of static distributions to extract the spectral diffusion dynamics as well as direct observation of coordinated hydrogen bonding solvation network rearrangements. Further, DMDC can be incorporated into different complex environments, providing a sensitive probe of local and global fluctuations with a high temporal dynamic range owing to the very long vibrational lifetime, even in strongly interacting solvents.

**Acknowledgment.** This work was supported by the National Science Foundation (CHE-0748501).

**Supporting Information Available:** Movies showing animations of the 10 carbonyl stretching vibrations. This material is available free of charge via the Internet at <http://pubs.acs.org>.

## References and Notes

- (1) Kwak, K.; Park, S.; Finkelstein, I. J.; Fayer, M. D. *J. Chem. Phys.* **2007**, *127*, 124503.
- (2) Elsaesser, T. *Acc. Chem. Res.* **2009**, *42*, 1220–1228.
- (3) Kim, Y. S.; Hochstrasser, R. *Proc. Natl. Acad. Sci. U.S.A.* **2005**, *102*, 11185–11190.
- (4) Asbury, J. B.; Steinel, T.; Stromberg, C.; Gaffney, K. J.; Piletic, I. R.; Goun, A.; Fayer, M. D. *Phys. Rev. Lett.* **2003**, *91*.
- (5) Asbury, J. B.; Steinel, T.; Stromberg, C.; Corcelli, S. A.; Lawrence, C. P.; Skinner, J. L.; Fayer, M. D. *J. Phys. Chem. A* **2004**, *108*, 1107–1119.
- (6) Asbury, J. B.; Steinel, T.; Fayer, M. D. *J. Phys. Chem. B* **2004**, *108*, 6544–6554.
- (7) Zheng, J. R.; Fayer, M. D. *J. Am. Chem. Soc.* **2007**, *129*, 4328–4335.
- (8) Fecko, C. J.; Eaves, J. D.; Loparo, J. J.; Tokmakoff, A.; Geissler, P. L. *Science* **2003**, *301*, 1698–1702.
- (9) Fecko, C. J.; Loparo, J. J.; Roberts, S. T.; Tokmakoff, A. *J. Chem. Phys.* **2005**, *122*, 054506.
- (10) Nicodemus, R. A.; Ramasesha, K.; Roberts, S. T.; Tokmakoff, A. *J. Phys. Chem. Lett.* **2010**, *1*, 1068–1072.
- (11) Roberts, S. T.; Ramasesha, K.; Tokmakoff, A. *Acc. Chem. Res.* **2009**, *42*, 1239–1249.
- (12) Bakker, H. J.; Skinner, J. L. *Chem. Rev.* **2010**, *110*, 1498–1717.
- (13) Stirnemann, G.; Laage, D. *J. Phys. Chem. Lett.* **2010**, *1*, 1511–1516.
- (14) Cho, M. *Chem. Rev.* **2008**, *108*, 1331–1418.
- (15) Woys, A. M.; Lin, Y. S.; Reddy, A. S.; Xiong, W.; de Pablo, J. J.; Skinner, J. L.; Zanni, M. T. *J. Am. Chem. Soc.* **2010**, *132*, 2832–2838.
- (16) Sengupta, N.; Maekawa, H.; Zhuang, W.; Toniolo, C.; Mukamel, S.; Tobias, D. J.; Ge, N. H. *J. Phys. Chem. B* **2009**, *113*, 12037–12049.
- (17) Ganim, Z.; Chung, H. S.; Smith, A. W.; Deflores, L. P.; Jones, K. C.; Tokmakoff, A. *Acc. Chem. Res.* **2008**, *41*, 432–441.
- (18) Ihalainen, J. A.; Paoli, B.; Muff, S.; Backus, E. H. G.; Bredenbeck, J.; Woolley, G. A.; Caflisch, A.; Hamm, P. *Proc. Natl. Acad. Sci. U.S.A.* **2008**, *105*, 9588–9593.
- (19) Zhuang, W.; Hayashi, T.; Mukamel, S. *Angew. Chem., Int. Ed.* **2009**, *48*, 3750–3781.
- (20) Schmidt, J. R.; Corcelli, S. A.; Skinner, J. L. *J. Chem. Phys.* **2004**, *121*, 8887–8896.
- (21) DeCamp, M. F.; DeFlores, L.; McCracken, J. M.; Tokmakoff, A.; Kwac, K.; Cho, M. *J. Phys. Chem. B* **2005**, *109*, 11016–11026.
- (22) Jansen, T. L. C.; Hayashi, T.; Zhuang, W.; Mukamel, S. *J. Chem. Phys.* **2005**, *123*, 114504.
- (23) Skinner, J. L.; Auer, B. M.; Lin, Y. S. *Adv. Chem. Phys.* **2009**, *142*, 59–103.
- (24) Paarmann, A.; Hayashi, T.; Mukamel, S.; Miller, R. J. D. *J. Chem. Phys.* **2009**, *130*, 204110.
- (25) Choi, J. H.; Oh, K. I.; Cho, M. H. *J. Chem. Phys.* **2008**, *129*, 174512.
- (26) Oh, K. I.; Choi, J. H.; Lee, J. H.; Han, J. B.; Lee, H.; Cho, M. *J. Chem. Phys.* **2008**, *128*, 154504.
- (27) Choi, J. H.; Oh, K. I.; Lee, H.; Lee, C.; Cho, M. *J. Chem. Phys.* **2008**, *128*, 134506.
- (28) Lindquist, B. A.; Furse, K. E.; Corcelli, S. A. *Phys. Chem. Chem. Phys.* **2009**, *11*, 8119–8132.
- (29) Lindquist, B. A.; Haws, R. T.; Corcelli, S. A. *J. Phys. Chem. B* **2008**, *112*, 13991–14001.
- (30) Lindquist, B. A.; Corcelli, S. A. *J. Phys. Chem. B* **2008**, *112*, 6301–6303.
- (31) Paarmann, A.; Hayashi, T.; Mukamel, S.; Miller, R. J. D. *J. Chem. Phys.* **2008**, *128*, 191103.
- (32) Jansen, T. L. C.; Auer, B. M.; Yang, M.; Skinner, J. L. *J. Chem. Phys.* **2010**, *132*, 7.
- (33) Lehtola, J.; Hakala, M.; Hamalainen, K. *J. Phys. Chem. B* **2010**, *114*, 6426–6436.
- (34) Tomsic, M.; Jamnik, A.; Fritz-Popovski, G.; Glatter, O.; Vlcek, L. *J. Phys. Chem. B* **2007**, *111*, 1738–1751.
- (35) Vahvaselka, K. S.; Serimaa, R.; Torkkeli, M. *J. Appl. Crystallogr.* **1995**, *28*, 189–195.
- (36) Wilson, K. R.; Cavalleri, M.; Rude, B. S.; Schaller, R. D.; Catalano, T.; Nilsson, A.; Saykally, R. J.; Pettersson, L. G. M. *J. Phys. Chem. B* **2005**, *109*, 10194–10203.
- (37) Abramavicius, D.; Palmieri, B.; Voronine, D. V.; Sanda, F.; Mukamel, S. *Chem. Rev.* **2009**, *109*, 2350–2408.
- (38) Bakalis, L. D.; Knoester, J. *J. Phys. Chem. B* **1999**, *103*, 6620–6628.
- (39) Knapp, E. W. *Chem. Phys.* **1984**, *85*, 73–82.
- (40) Didraga, C.; Knoester, J. *Chem. Phys.* **2002**, *275*, 307–318.
- (41) Mukamel, S.; Tretiak, S.; Wagersreiter, T.; Chernyak, V. *Science* **1997**, *277*, 781–787.
- (42) Dahlbom, M.; Pullerits, T.; Mukamel, S.; Sandström, V. *J. Phys. Chem. B* **2001**, *105*, 5515–5524.
- (43) Laage, D.; Hynes, J. T. *Science* **2006**, *311*, 832–835.
- (44) Nee, M. J.; Baiz, C. R.; Anna, J. M.; McCanne, R.; Kubarych, K. J. *J. Chem. Phys.* **2008**, *129*, 084503.
- (45) Baiz, C. R.; Nee, M. J.; McCanne, R.; Kubarych, K. J. *Opt. Lett.* **2008**, *33*, 2533–2535.
- (46) Baiz, C. R.; McRobbie, P. L.; Anna, J. M.; Geva, E.; Kubarych, K. J. *Acc. Chem. Res.* **2009**, *42*, 1395–1404.
- (47) Baiz, C. R.; McRobbie, P. L.; Preketes, N. K.; Kubarych, K. J.; Geva, E. *J. Phys. Chem. A* **2009**, *113*, 9617–9623.
- (48) Baiz, C. R.; McCanne, R.; Nee, M. J.; Kubarych, K. J. *J. Phys. Chem. A* **2009**, *113*, 8907–8916.
- (49) Davydov, A. S. *Theory of Molecular Excitons*; McGraw-Hill: New York, 1962.
- (50) Pullerits, T.; Chachisvilis, M.; Sundström, V. *J. Phys. Chem.* **1996**, *100*, 10787–10792.
- (51) Krueger, B. P.; Scholes, G. D.; Fleming, G. R. *J. Phys. Chem. B* **1998**, *102*, 9603–9603.
- (52) van Amerongen, H.; van Grondelle, R. *J. Phys. Chem. B* **2001**, *105*, 604–617.
- (53) Durrant, J. R.; Knoester, J.; Wiersma, D. A. *Chem. Phys. Lett.* **1994**, *222*, 450–456.
- (54) Kano, H.; Kobayashi, T. *Bull. Chem. Soc. Jpn.* **2002**, *75*, 1071–1074.
- (55) Dijkstra, A. G.; Jansen, T. L. C.; Knoester, J. *J. Chem. Phys.* **2008**, *128*, 164511.
- (56) Milota, F.; Sperling, J.; Nemeth, A.; Kauffmann, H. F. *Chem. Phys.* **2009**, *357*, 45–53.
- (57) Womick, J. M.; Miller, S. A.; Moran, A. M. *J. Phys. Chem. A* **2009**, *113*, 6587–6598.
- (58) Collini, E.; Scholes, G. D. *Science* **2009**, *323*, 369–373.
- (59) Anderson, P. W. *Phys. Rev.* **1958**, *109*, 1492–1505.
- (60) Thouless, D. J. *Phys. Rep.* **1974**, *13*, 50.
- (61) Knoester, J. *Phys. Rev. A* **1993**, *47*, 2083–2098.
- (62) Faeder, S. M. G.; Jonas, D. M. *J. Phys. Chem. A* **1999**, *103*, 10489–10505.
- (63) Hybl, J. D.; Christophe, Y.; Jonas, D. M. *Chem. Phys.* **2001**, *266*, 295–309.

- (64) Khalil, M.; Demirdoven, N.; Tokmakoff, A. *Phys. Rev. Lett.* **2003**, *90*, 047401.
- (65) Khalil, M.; Demirdoven, N.; Tokmakoff, A. *J. Phys. Chem. A* **2003**, *107*, 5258–5279.
- (66) Roberts, S. T.; Loparo, J. J.; Tokmakoff, A. *J. Chem. Phys.* **2006**, *125*, 084502.
- (67) CRC Handbook of Chemistry and Physics; CRC Press: Boca Raton, 1984.
- (68) Kwak, K.; Rosenfeld, D. E.; Fayer, M. D. *J. Chem. Phys.* **2008**, *128*, 204505.
- (69) Kuroda, D. G.; Vorobyev, D. Y.; Hochstrasser, R. M. *J. Chem. Phys.* **2010**, *132*, 044501.
- (70) Nee, M. J.; McCanne, R.; Kubarych, K. J.; Joffre, M. *Opt. Lett.* **2007**, *32*, 713–715.
- (71) Ogilvie, J. P.; Kubarych, K. J. *Adv. At. Mol. Opt. Phys.* **2009**, *57*, 249–321.
- (72) Anna, J. M.; Nee, M. J.; Baiz, C. R.; McCanne, R.; Kubarych, K. J. *J. Opt. Soc. Am. B* **2010**, *27*, 382–393.
- (73) Lee, K. F.; Nuernberger, P.; Bonalet, A.; Joffre, M. *Opt. Express* **2009**, *17*, 18738–18744.
- (74) Schmidt, J. R.; Corcelli, S. A.; Skinner, J. L. *J. Chem. Phys.* **2004**, *121*, 8887–8896.
- (75) Jansen, T. L. C.; Knoester, J. *J. Chem. Phys.* **2007**, *127*, 234502.
- (76) Jansen, T. L. C.; Knoester, J. *Biophys. J.* **2008**, *94*, 1818–1825.
- (77) Jansen, T. L. C.; Knoester, J. *Acc. Chem. Res.* **2009**, *42*, 1405–1411.
- (78) Kwac, K.; Lee, C.; Jung, Y.; Han, J.; Kwak, K.; Zheng, J. R.; Fayer, M. D.; Cho, M. *J. Chem. Phys.* **2006**, *125*, 244508.
- (79) Sanda, F.; Zhuang, W.; Jansen, T. L. C.; Hayashi, T.; Mukamel, S. *Ultrafast Phenomena XV* **2007**, *88*, 401–403.
- (80) Stewart, A. I.; Clark, I. P.; Towrie, M.; Ibrahim, S. K.; Parker, A. W.; Pickett, C. J.; Hunt, N. T. *J. Phys. Chem. B* **2008**, *112*, 10023–10032.
- (81) Bonner, G. M.; Ridley, A. R.; Ibrahim, S. K.; Pickett, C. J.; Hunt, N. T. *Faraday Discuss.* **2010**, *145*, 429–442.
- (82) Baiz, C. R.; McRobbie, P. L.; Prekete, N. K.; Kubarych, K. J.; Geva, E. *J. Phys. Chem. A* **2009**, *113*, 9617–9623.
- (83) Chernyak, V.; Zhang, W. M.; Mukamel, S. *J. Chem. Phys.* **1998**, *109*, 9587–9601.
- (84) Gharavi, M.; Buckley, S. G. *Appl. Spectrosc.* **2004**, *58*, 468–473.
- (85) Vlaming, S. M.; Malyshev, V. A.; Knoester, J. *Phys. Rev. B* **2009**, *79*, 205121.
- (86) Zhuang, W.; Abramavicius, D.; Hayashi, T.; Mukamel, S. *J. Phys. Chem. B* **2006**, *110*, 3362–3374.
- (87) Piletic, I. R.; Moilanen, D. E.; Levinger, N. E.; Fayer, M. D. *J. Am. Chem. Soc.* **2006**, *128*, 10366–10367.
- (88) Anna, J. M.; Ross, M. R.; Kubarych, K. J. *J. Phys. Chem. A* **2009**, *113*, 6544–6547.
- (89) Engel, G. S.; Calhoun, T. R.; Read, E. L.; Ahn, T. K.; Mančal, T.; Cheng, Y. C.; Blankenship, R. E.; Fleming, G. R. *Nature* **2007**, *446*, 782–786.
- (90) Collini, E.; Wong, C. Y.; Wilk, K. E.; Curmi, P. M. G.; Brumer, P.; Scholes, G. D. *Nature* **2010**, *463*, 644–U669.
- (91) Jansen, T. L. C.; Cringus, D.; Pshenichnikov, M. S. *J. Phys. Chem. A* **2009**, *113*, 6260–6265.
- (92) Anna, J. M.; Nee, M. J.; Baiz, C. R.; McCanne, R.; Kubarych, K. J. *J. Opt. Soc. Am. B* **2010**, *27*, 382–393.
- (93) Tielrooij, K. J.; Garcia-Araez, N.; Bonn, M.; Bakker, H. *J. Science* **2010**, *328*, 1006–1009.
- (94) Ji, M. B.; Odelius, M.; Gaffney, K. J. *Science* **2010**, *328*, 1003–1005.
- (95) Press, W. H.; Teukolsky, S. A.; Vetterling, W. T.; Flannery, B. P. *Numerical Recipes in C*, 2nd ed.; Cambridge University Press: Cambridge, 1992.
- (96) Tekavec, P. E.; Myers, J. A.; Lewis, K. L. M.; Ogilvie, J. P. *Opt. Lett.* **2009**, *34*, 1390–1392.
- (97) Cho, B.; Yetzbacher, M. K.; Kitney, K. A.; Smith, E. R.; Jonas, D. M. *J. Phys. Chem. A* **2009**, *113*, 13287–13299.
- (98) Kwak, K. W.; Park, S.; Fayer, M. D. *Proc. Natl. Acad. Sci. U.S.A.* **2007**, *104*, 14221–14226.
- (99) Kim, Y. S.; Hochstrasser, R. M. *J. Phys. Chem. B* **2007**, *111*, 9697–9701.
- (100) Garrett-Roe, S.; Hamm, P. *Acc. Chem. Res.* **2009**, *42*, 1412–1422.
- (101) Garrett-Roe, S.; Hamm, P. *J. Chem. Phys.* **2009**, *130*, 164510.
- (102) Guo, J. H.; Luo, Y.; Augustsson, A.; Kashtanov, S.; Rubensson, J. E.; Shuh, D. K.; Ågren, H.; Nordgren, J. *Phys. Rev. Lett.* **2003**, *91*, 4.
- (103) Stewart, G. W.; Morrow, R. M. *Phys. Rev.* **1927**, *30*, 232–244.
- (104) Stewart, G. W.; Skinner, E. W. *Phys. Rev.* **1928**, *31*, 1–9.
- (105) Narten, A. H.; Habenschuss, A. *J. Chem. Phys.* **1984**, *80*, 3387–3391.

JP106142U